# Statistical Analysis of Small Bubble Dynamics in Isotropic Turbulence

Murray R. Snyder[1], Omar M. Knio[2], Joseph Katz[3] and and Olivier P. Le Maître[4]

[1,2,3]Department of Mechanical Engineering
The Johns Hopkins University
Baltimore, MD 21218-2686, USA

[4]Laboratoire de Mécanique et d'Energétique d'Evry
&
Laboratoire d'Informatique pour la Mécanique et les Sciences de l'Ingénieur
Université d'Evry Val d'Essonne
40, rue du Pelvoux, CE 1455
91020 Evry cedex, France

Submitted to:
*Physics of Fluids*

**Key Words:** Turbulence, Bubbles, Rise Velocity, Dispersion

[1]Corresponding author. Present address: Department of Mechanical Engineering, The United States Naval Academy, Annapolis, Maryland 21402-5042; Email: msnyder@usna.edu
[2]Email: knio@jhu.edu
[3]Email: katz@jhu.edu
[4]Email: olm@iup.univ-evry.fr

**Suggested Running Head:** Bubble dynamics in isotropic turbulence

**Mailing Address:** Murray R. Snyder
Department of Mechanical Engineering
The United States Naval Academy
590 Holloway Road
Annapolis, MD 21402-5042
Phone: (410) 533-8046; Fax: (410) 293-3041
Email: msnyder@usna.edu

# ABSTRACT

The dynamics and dispersion of small air bubbles in isotropic turbulence are analyzed computationally. The flow field is simulated using a pseudo-spectral code, while the bubble dynamics are analyzed by integration of a Lagrangian equation of motion that accounts for buoyancy, added mass, pressure, drag, and lift forces. Probability density functions (pdfs) of bubble velocities, lift and drag forces, and of field velocities and vorticities along bubble trajectories are used to analyze bubble dynamics. Lagrangian bubble trajectories are also employed to determine dispersion characteristics, following the theoretical development of Cushman and Moroni (2001). Consistent with available experimental data, bubble rise velocities are increasingly suppressed with increasing turbulence intensity. The analysis also reveals that the vertical bubble velocities are characterized by asymmetric pdfs that are positive or negative-skewed dependent upon the non-dimensional turbulence intensity and the Taylor length scale. The role of the lift force in moving the bubbles to the down-flow side of turbulent eddies, and consequently retarding their rise, is consistently observed in all analysis. The dispersion of 40 $\mu$m bubbles and transition to Fickian behavior is shown to be weakly affected by the turbulence level. Larger, 400 $\mu$m bubbles are shown to be more sensitive to turbulence level with transition to Fickian behavior delayed in low turbulence fields.

# 1 Introduction

The behavior of small particles, bubbles and droplets in turbulent flows is important to numerous physical processes including, among other examples, the production, refining and distribution of oil products, and the environmental monitoring and cleanup of contaminants. It is generally accepted that the rise of bubbles is suppressed by turbulence (Wang and Maxey [1], Spelt and Biesheuvel [2], Poorte and Biesheuvel[3]). Conversely, it also accepted that the settling of heavy particles is enhanced by turbulence (Maxey[4], Wang and Maxey[5], Mei[6]).

Numerous mechanisms have been analyzed that contribute to, or affect the turbulent enhancement of heavy particle settling and the retardation of bubble rise rates. These include "trajectory biasing," lift forces, and non-linear drag. Trajectory biasing has been shown (Maxey[4], Wang and Maxey[5], Mei [6]) to increase the settling velocity of particles heavier than the surrounding fluid by preferentially sweeping them to the down-flow sides of turbulent eddies. Wang and Maxey[1] show that, conversely, trajectory biasing reduces bubble rise velocity.

Non-linear drag has been shown to be a significant factor affecting both the settling rate of heavy particles and rise rate of bubbles when particle or bubble Reynolds numbers are above the Stokes flow regime ($Re_p$ or $Re_b > 1$) where $Re_p = \frac{2\boldsymbol{U}\tilde{a}}{\tilde{\nu}}$, $\boldsymbol{U}$ is velocity, $\tilde{a}$ is radius and $\tilde{\nu}$ is kinematic viscosity. Numerous studies (Tunstall and Houghton[7], Hwang[8], Fung[9;10], Mei[6], Stout *et al.*[11], Mei *et al.*[12]) have noted that the non-linear increase of the drag force when $Re_p \gg 1$ may result in a reduction of the mean settling velocity of heavy particles, though this effect may be counteracted by trajectory biasing for small particles, particularly when the particle diameter is much smaller than the Kolmogorov microscale.

The role of the lift forces in retarding the rise of bubbles has also been analyzed. In particular, Spelt and Biesheuvel[2;13] used numerical simulation to show that lift forces reduced the rise velocity of bubbles in isotropic turbulence by preferentially moving bubbles horizontally towards regions of net downward fluid velocity.

Inconsistent with the trends observed for bubbles and heavy particles, recent experimental work by Friedman and Katz[14], showed surprising behavior for fuel droplets that are slightly lighter than water. Specifically, the mean rise velocity in turbulence was found to be larger or smaller than the quiescent rise velocity, depending upon the turbulence intensity, droplet size and upon the droplet Stokes number $St_d$. The present paper is part of an effort aiming at explaining this unexpected behavior in particular, and more generally at investigating dispersion of bubbles and droplets in turbulent flow fields.

In the present phase of the effort, attention is focused exclusively on the behavior of air bubbles in isotropic turbulent flows. Specific objectives include establishment of confidence in the validity of the numerical predictions, characterization of the mean bubble rise and investigation of the origin of observed trends, and detailed analysis of the bubble dispersion process and its (statistical)

dependence on length and time scales.

Our present focus on the behavior of bubbles is motivated in part by the availability of a large body of experimental and computational data on the rise of air bubbles in isotropic turbulence, and of useful correlations of the forces experienced by bubbles in relevant vorticity dominated flows.[15;16] As further discussed in Section 2, the present approach is based on a one-way coupling model, which combines a direct solver for single-phase flow, with a Lagrangian tracking of the bubble motion. Specifically, the bubbles are tracked by integrating a Lagrangian equation of motion that accounts for drag, lift, added mass and pressure forces. Though the model ignores the effect of bubbles on the turbulent flow field, it enables us to efficiently consider a wide parameter regime, which facilitates the analysis of bubble rise and dispersion.

In section 3, the numerical model is applied to analyze the rise of small bubbles in isotropic turbulence. Specifically, the mean rise of the bubbles is determined for different turbulence conditions and different bubble diameters. Consistent with relevant experimental and computational data, in all cases one observes a suppression of the mean bubble rise from the corresponding quiescent rise velocity. In order to further characterize the observed trends, a statistical analysis is performed of the bubble velocities, bubble Reynolds numbers, the flow vorticity at the bubble positions, as well as the drag and lift forces experienced by the bubbles.

In section 4, the computed results are once again exploited to conduct a detailed analysis of the bubble dispersion process. The analysis relies on the recent theoretical development of Cushman and Moroni[17;18], who introduce a time- and lengthscale-dependent dispersion tensor. The theory generalizes the classical Fickian theory in which the dispersion rate is described using a single scalar. The generalized theory is applied to (i) explore conditions under which the bubble dispersion can be well approximated by a Fickian process, (ii) characterize, for different bubble diameters, the effect of the dissipation rate on the bubble dispersion, and (iii) where appropriate, establish links between the generalized and classical dispersion theories. Comparison is made with the experimental results of Snyder and Lumley[19], Spelt and Biesheuvel[2] and Mazzitelli and Lohse.[20]

Major conclusions are provided in section 5.

# 2 Formulation and Numerical Scheme

## 2.1 Governing Equations for the Flow

Consider the turbulent flow in a cubic periodic domain with side-length $\widetilde{L}$. The fluid is assumed incompressible with uniform density, $\rho$, and dynamic viscosity, $\mu$. The flow in the domain $\widetilde{\mathcal{D}} \equiv [0, \widetilde{L}]^3$ is governed by the momentum and mass conservation equations:[21]

$$\begin{cases} \rho \dfrac{\partial \boldsymbol{U}}{\partial \tilde{t}} + \rho \boldsymbol{U} \widetilde{\boldsymbol{\nabla}} \boldsymbol{U} = -\widetilde{\boldsymbol{\nabla}} P + \mu \widetilde{\nabla}^2 \boldsymbol{U} + \rho \boldsymbol{G} + \rho \boldsymbol{F}, \\ \widetilde{\boldsymbol{\nabla}} \cdot \boldsymbol{U} = 0. \end{cases} \tag{1}$$

where $\boldsymbol{U}$ is the velocity vector, $\tilde{t}$ is time, $P$ is pressure, and $\boldsymbol{G}$ and $\boldsymbol{F}$ denote the gravity and applied force per unit volume, respectively. Where necessary, tildes are used to denote dimensional quantities.

Using $L^c \equiv \widetilde{L}/2\pi$ as characteristic length scale, and $U^c \equiv \alpha(\tilde{\nu}/L^c)$ as characteristic velocity scale, one can define normalized values of velocity, length, pressure, time, gravity force and applied force as follows:

$$\boldsymbol{u} = \boldsymbol{U}/U^c,\ \boldsymbol{x} = \boldsymbol{X}/L^c,\ p \equiv \frac{P}{\rho (U^c)^2},\ t \equiv \frac{\tilde{t} U^c}{L^c},\ \boldsymbol{g} \equiv \frac{\boldsymbol{G} L^c}{(U^c)^2},\ \boldsymbol{f} \equiv \frac{\boldsymbol{F} L^c}{(U^c)^2}\ .$$

Here, $\alpha$ is a constant, and $\tilde{\nu} \equiv \tilde{\mu}/\tilde{\rho}$ is the kinematic viscosity. Using this normalization convention, the normalized governing equations may be expressed as:

$$\begin{cases} \dfrac{\partial \boldsymbol{u}}{\partial t} + \boldsymbol{u} \boldsymbol{\nabla} \boldsymbol{u} = -\boldsymbol{\nabla} p + \dfrac{1}{\mathrm{Re}} \nabla^2 \boldsymbol{u} + \boldsymbol{g} + \boldsymbol{f}, \\ \boldsymbol{\nabla} \cdot \boldsymbol{u} = 0, \end{cases} \tag{2}$$

where $\mathrm{Re} \equiv U^c L^c / \nu = \alpha$ is the "nominal" Reynolds number.

## 2.2 Direct numerical simulation of the flow

A pseudo-spectral flow solver is used to simulate the evolution of the flow. The solver is based on integration of normalized mass and momentum equations:

$$\begin{cases} \dfrac{\partial \boldsymbol{u}}{\partial t} + \boldsymbol{\omega} \wedge \boldsymbol{u} = -\boldsymbol{\nabla} p^* + \dfrac{1}{\mathrm{Re}} \nabla^2 \boldsymbol{u} + \boldsymbol{f}, \\ \boldsymbol{\nabla} \cdot \boldsymbol{u} = 0, \end{cases} \tag{3}$$

with periodic boundary conditions on the domain $\mathcal{D} = [0, 2\pi]^3$. Here $p^* \equiv p + \phi_g + \frac{1}{2}\|\boldsymbol{u}^2\|$ is the normalized total head, where $\phi_g$ is the gravitational potential, defined such that $\boldsymbol{g} \equiv \boldsymbol{\nabla} \phi_g$.

The pseudo-spectral scheme of Vincent and Meneguzzi[22] is adapted to the simulation of (3). Briefly, taking the Fourier transform of the governing equations, one obtains:

$$\begin{cases} \left(\dfrac{d}{dt} + \dfrac{\boldsymbol{k}\cdot\boldsymbol{k}}{\mathrm{Re}}\right)\hat{\boldsymbol{u}}_{\boldsymbol{k}} = -i\boldsymbol{k}\widehat{p^*}_{\boldsymbol{k}} + (\widehat{\boldsymbol{u}\wedge\boldsymbol{\omega}})_{\boldsymbol{k}} + \hat{\boldsymbol{f}}_{\boldsymbol{k}}, \\ i\boldsymbol{k}\cdot\hat{\boldsymbol{u}}_{\boldsymbol{k}} = 0. \end{cases} \tag{4}$$

where hats are used to denote the Fourier coefficients. Equation (4) is advanced in time using a mixed integration scheme, in which the non-linear term is treated explicitly using a second-order Adams-Bashforth method, while the diffusion term is handled using exact factorization. This discretization results in the following equation for each wave-vector $\boldsymbol{k}$:

$$\begin{aligned} \hat{\boldsymbol{u}}_{\boldsymbol{k}}^{n+1} &= \hat{\boldsymbol{u}}_{\boldsymbol{k}}^{n}\, e^{-\frac{k^2}{\mathrm{Re}}\Delta t} + \Delta t\boldsymbol{P}\left[\hat{\boldsymbol{f}}_{\boldsymbol{k}}^{n}\, e^{-\frac{k^2}{\mathrm{Re}}\Delta t}\right] \\ &+ \Delta t\boldsymbol{P}\left[\frac{3}{2}(\widehat{\boldsymbol{u}\wedge\boldsymbol{\omega}})_{\boldsymbol{k}}^{n}\, e^{-\frac{k^2}{\mathrm{Re}}\Delta t} - \frac{1}{2}(\widehat{\boldsymbol{u}\wedge\boldsymbol{\omega}})_{\boldsymbol{k}}^{n-1}\, e^{-2\frac{k^2}{\mathrm{Re}}\Delta t}\right], \end{aligned} \tag{5}$$

where the superscript refers to the time level, $\Delta t$ is the time step, $k^2 \equiv \boldsymbol{k}\cdot\boldsymbol{k}$, and $\boldsymbol{P}[\cdot]$ denotes the projector onto the direction perpendicular to $\boldsymbol{k}$.

The non-linear terms in (5) are evaluated in a pseudo-spectral fashion[23]. No de-aliasing procedure is applied, but a spherical truncation is used[24]. Finally, the forcing term $\boldsymbol{f}$, which is necessary to sustain the turbulence, is set as

$$\hat{\boldsymbol{f}}_{\boldsymbol{k}} = \frac{\epsilon}{26}\frac{\hat{\boldsymbol{u}}_{\boldsymbol{k}}}{|\hat{\boldsymbol{u}}_{\boldsymbol{k}}|^2} \text{ for } 0 < \|\boldsymbol{k}\| < 2, \quad \hat{\boldsymbol{f}}_{\boldsymbol{k}} = 0 \text{ otherwise.} \tag{6}$$

Thus, constant energy injection with rate rate $\epsilon$ is imposed. After an initial transition, the dissipation rates oscillates slightly around $\epsilon$.

The turbulent flow has two relevant dimensionless physical parameters, the nominal Reynolds number, Re, which is set to 1000, and the reduced dissipation rate, $\epsilon$ ($=4.0\text{x}10^{-3}$). These parameters fix the normalized Kolmogorov microscale: $\eta \equiv \left(\epsilon\mathrm{Re}^3\right)^{-1/4} \approx 0.022$.

## 2.3 Governing Equations for Bubble Motion

We assume that the bubbles are small, such that surface tension prevents significant deformations. Thus, the bubbles remain spherical with constant radius $\tilde{a}$. Furthermore, we assume a small void fraction so that the bubbles do not impact the turbulent field; bubble-bubble interactions are also ignored.

Following Maxey & Riley[25], the dimensional equations of motion for a bubble are given by:[26;16;27;28]

$$\begin{cases} \dfrac{d\boldsymbol{X}_b}{d\tilde{t}} = \boldsymbol{V}_b(\tilde{t}), \\ \dfrac{d\boldsymbol{V}_b}{d\tilde{t}} = -2\Delta\rho^*\boldsymbol{G} - 2\rho^*\boldsymbol{F} + 3\rho^*\dfrac{D\boldsymbol{U}}{D\tilde{t}} + \dfrac{3\rho^*}{4\tilde{a}}\left[C_D\|\boldsymbol{U}_r\|\boldsymbol{U}_r + C_L\dfrac{\|\boldsymbol{U}_r\|}{\|\tilde{\boldsymbol{\omega}}\|}\boldsymbol{U}_r\wedge\tilde{\boldsymbol{\omega}}\right], \end{cases} \tag{7}$$

where $\boldsymbol{X}_b(\tilde{t})$, $\boldsymbol{V}_b(\tilde{t})$, and $\rho_b$ respectively denote the bubble position, velocity, and density,

$$\rho^* \equiv \frac{\rho}{2\rho_b+\rho}, \tag{8}$$

is the reduced density,

$$\Delta\rho^* \equiv \frac{\rho-\rho_b}{2\rho_b+\rho}. \tag{9}$$

is the reduced density difference, $\tilde{\boldsymbol{\omega}} = \widetilde{\boldsymbol{\nabla}}\wedge\boldsymbol{U}$ is the local vorticity at the bubble position (see further discussion below), $\boldsymbol{U}_r \equiv \boldsymbol{U}(\boldsymbol{X}_b(\tilde{t}),\tilde{t}) - \boldsymbol{V}_b(\tilde{t})$ is the relative velocity.

The lift coefficient $C_L$ is adapted from the experimental correlations of Sridhar and Katz[16]. Specifically, we set:

$$C_L = 0.59\left(\frac{\tilde{a}\|\tilde{\boldsymbol{\omega}}\|}{\|\boldsymbol{U}_r\|}\right)^{1/4}. \tag{10}$$

Following Cerutti *et al.*[26], the following correlation is used for the drag coefficient:

$$\begin{cases} C_D = \dfrac{24}{Re_b}, \quad Re_b < 1, \\ C_D = \left(\dfrac{24}{Re_b}\right)\left(1+\dfrac{3.6}{Re_b^{0.313}}\left(\dfrac{Re_b-1}{19}\right)^2\right), \quad 1\le Re_b\le 20, \\ C_D = \left(\dfrac{24}{Re_b}\right)\left(1+.15Re_b^{0.687}\right), \quad Re_b > 20, \end{cases} \tag{11}$$

where

$$\mathrm{Re}_b = \frac{2\tilde{a}\|\boldsymbol{U}_r\|}{\nu}. \tag{12}$$

The equations of motion of the bubbles are normalized using the same characteristic scales as in the normalization of the flow equations. This results in:

$$\begin{cases} \dfrac{d\boldsymbol{x}_b}{dt} = \boldsymbol{v}_b(t), \\ \dfrac{d\boldsymbol{v}_b}{dt} = -2\Delta\rho^*\boldsymbol{g} - 2\rho^*\boldsymbol{f} + 3\rho^*\dfrac{D\boldsymbol{u}}{Dt} + \dfrac{3\rho^*}{4a}\left[C_D\|\boldsymbol{u}_r\|\boldsymbol{u}_r + C_L\dfrac{\|\boldsymbol{u}_r\|}{\|\boldsymbol{\omega}\|}\boldsymbol{u}_r\wedge\boldsymbol{\omega}\right], \end{cases} \tag{13}$$

where $a = \tilde{a}/L^c$ is the normalized bubble radius, and

$$\mathrm{Re}_b = 2a\|\boldsymbol{u}_r\|\mathrm{Re} \tag{14}$$

is the bubble Reynolds number. In terms of dimensionless quantities, the lift coefficient is given by:

$$C_L = 0.59\left(\frac{a\|\boldsymbol{\omega}\|}{\|\boldsymbol{u}_r\|}\right)^{1/4} \tag{15}$$

where $\boldsymbol{\omega}$ is the normalized vorticity.

The normalized fluid Lagrangian acceleration is determined from the inverse Fourier transform of the corresponding modes:

$$\left(\widehat{\frac{D\boldsymbol{u}}{Dt}}\right)_{\boldsymbol{k}} = -i\boldsymbol{k}(\widehat{p+\phi_g})_{\boldsymbol{k}} - \frac{k^2}{\mathrm{Re}}\hat{\boldsymbol{u}}_{\boldsymbol{k}} + \hat{\boldsymbol{f}}_{\boldsymbol{k}}, \tag{16}$$

where

$$(\widehat{p+\phi_g})_{\boldsymbol{k}} = \frac{-i\boldsymbol{k}}{k^2}\cdot\left[(\widehat{\boldsymbol{u}\wedge\boldsymbol{\omega}})_{\boldsymbol{k}} + \hat{f}_{\boldsymbol{k}}\right] - \frac{1}{2}\,(\widehat{\boldsymbol{u}\cdot\boldsymbol{u}})_{\boldsymbol{k}}\,. \tag{17}$$

Note that since the density of the bubbles is much smaller than that of the fluid, i.e. $\rho_b << \rho$, we have $\rho^* \approx 1$ and $\Delta\rho^* \approx 1$. Thus, the equations of motion of the bubbles reduce to:

$$\begin{cases} \dfrac{d\boldsymbol{x}_b}{dt} = \boldsymbol{v}_b(t), \\ \dfrac{d\boldsymbol{v}_b}{dt} = -2(\boldsymbol{g}+\boldsymbol{f}) + 3\dfrac{D\boldsymbol{u}}{Dt} + \dfrac{3}{4a}\left[C_D\|\boldsymbol{u}_r\|\boldsymbol{u}_r + C_L\dfrac{\|\boldsymbol{u}_r\|}{\|\boldsymbol{\omega}\|}\boldsymbol{u}_r\wedge\boldsymbol{\omega}\right], \end{cases} \tag{18}$$

which, except for the forcing term, is identical to the expression used by Sridhar and Katz[16;27].

## 2.4 Integration of the Equation of Motion

Integration of the equations of motion is performed using the implicit-explicit (IMEX) approach developed by Cerutti *et al.*[26]. The approach is based on an implicit, Crank-Nicolson treatment of the linear part of the drag term, and on explicit treatment of the remaining terms. The advantage of this approach is that it overcomes the inherent stiffness of the equation of motion, which arises as the bubble Reynolds number is small.

Implementation of this approach is based on first rewriting the bubble acceleration as:

$$\frac{d\boldsymbol{v}_b}{dt} = H(t) + \frac{3\rho^*}{4a}\frac{24}{\mathrm{Re}_b}\|\boldsymbol{u}_r\|\boldsymbol{u}_r, \tag{19}$$

where

$$H(t) \equiv -2\Delta\rho^*\boldsymbol{g} - 2\rho^*\boldsymbol{f} + 3\rho^*\frac{D\boldsymbol{u}}{Dt} + \frac{3\rho^*}{4a}\left[\left(C_D - \frac{24}{\mathrm{Re}_b}\right)\|\boldsymbol{u}_r\|\boldsymbol{u}_r + C_L\frac{\|\boldsymbol{u}_r\|}{\|\boldsymbol{\omega}\|}\boldsymbol{u}_r\wedge\boldsymbol{\omega}\right]. \tag{20}$$

Substituting the expression for $\mathrm{Re}_b$ into (19), we get:

$$\frac{d\boldsymbol{v}_b}{dt} = H(t) + \frac{9\rho^*}{a^2\mathrm{Re}}(\boldsymbol{u} - \boldsymbol{v}_b). \tag{21}$$

In the computations, the first term is integrated explicitly using a third order Adams-Bashforth scheme, while the second term is treated implicitly using a Crank-Nicolson scheme. The velocity update is thus expressed as:

$$\boldsymbol{v}_b^{n+1} = \frac{\boldsymbol{v}_b^n + \Delta t\left(\bar{H} + \bar{G} + \dfrac{9\rho^*}{2a^2\mathrm{Re}}\boldsymbol{u}^{n+1}\right)}{1 + \dfrac{9\rho^*}{2a^2\mathrm{Re}}\Delta t}, \tag{22}$$

where

$$\bar{H} \equiv \frac{23}{12}H^n - \frac{16}{12}H^{n-1} + \frac{5}{12}H^{n-2}, \tag{23}$$

$$\bar{G} \equiv \frac{9\rho^*}{2a^2\mathrm{Re}}(\boldsymbol{u}^n - \boldsymbol{v}_b^n). \tag{24}$$

Note that the flow velocity at the new time step, $\boldsymbol{u}^{n+1}$, appears on the right-hand side of (22). Thus, the flow field is updated first, and the equations of motion of the bubbles are updated second in order to complete an integration step.

# 3 Bubble Rise Results

## 3.1 Data Generation and Methodology

Results are obtained for air bubbles rising in four different isotropic turbulent fields having different characteristics, as summarized in Table 1. In all cases, the fluid is water with $\tilde{\rho} = 1000$ kg/m$^3$ and $\tilde{\nu} = 10^{-6}$ m$^2$/s. Normal gravity is assumed to prevail with $\tilde{g} = 9.8$ m/s$^2$.

The flow is computed using the scheme outlined in section 2 with $128^3$ grid points. The simulations are performed by first integrating the flow conservation equations over a period sufficiently long for a stationary isotropic turbulent flow field to be obtained, as verified by monitoring the spectrum of the turbulent kinetic energy.

Once stationary turbulence is reached, a set of bubbles is injected in the flow. We take advantage of the one-way coupling model by injecting a large number of bubbles of different radii in the range of 5-600 $\mu$m. For each radius, a set of 5000 bubbles is considered; their initial locations are drawn at random from a uniform distribution over the domain, and their initial velocity coincides with the local flow velocity at the bubble center. The motion of the bubbles is then tracked by integrating the Lagrangian equations of motion outlined above. In order to minimize the impact of the prescribed initial bubble position and velocity, the motion of the bubbles for a period of $t = 50$ after injection is discarded, and data collection and analysis is performed for $50 \leq t \leq 250$ following bubble injection. The position and velocity of the bubbles as well as flow velocity and vorticity at the bubbles' center are recorded periodically at a fine time interval, $\delta t = 0.1$.

Analysis of the bubble dynamics and dispersion based on the resulting data is discussed in the following sections. For brevity, we focus most of our attention on two data sets: "small bubbles" with radius of 40 $\mu$m and "large bubbles" with 400 $\mu$m radius. In section 3.2 the mean rise velocity of the bubbles is examined, and contrasted with corresponding predictions for quiescent conditions. A more detailed analysis of the dynamics is then performed in section 3.3, where statistical distributions of the bubble velocity, local flow and relative velocity, vorticity and fluid forces experienced by the bubbles along their paths are generated. These distributions are used to further characterize the trends in the mean rise observed earlier.

## 3.2 Mean Bubble Rise

### 3.2.1 Suppression of Rise Velocity

Figure 1 and Table 2 provide a comparison of the computed bubble rise rates in turbulence with those calculated for quiescent conditions. The results show an increasing suppression of the bubble rise velocity (w.r.t the quiescent value) as the turbulence level increases. For all fields studied, the amount of rise velocity suppression increases as bubble radius increased. Note that the shape of the

quiescent rise curve between 100 and 225 $\mu$m radius is affected by the numerical approximation used for the transition between different drag coefficient regimes, namely from the Stokes flow regime ($Re_b < 1$) to the empirical correlation for $Re_b > 20$ (11).

The turbulence magnitude is often measured using the relative turbulence intensity $\beta$. Two definitions are found in the literature, $\beta = \frac{\sqrt{u'^2}}{|u_r|}$ or $\beta = \frac{\sqrt{u'^2}}{|u_t|}$, where $u'$ is root mean square of the flow velocity fluctuation, $|u_r|$ is the magnitude of the mean relative velocity between the bubble and the turbulent flow, and $|u_t|$ is the magnitude of the bubble terminal velocity in a quiescent fluid. In the following, we shall use the definition based on the terminal velocity.

Based on the results in Figure 1, our reduction in rise velocity ranges from approximately 20% for turbulent fields 3 and 4 (with $\beta < 0.5$ for bubble radius $\geq$ 240 $\mu$m) to approximately 60% for highest turbulence field 1 (with $\beta > 2$ for bubble radius $\geq$ 240 $\mu$m). In all fields, larger bubbles experienced more reduction in rise velocity than smaller ones. These results are consistent with available computational and experimental data. For example, computations by Wang and Maxey[1] show an approximately 33% decrease in microbubble rise velocities for $\beta \gg 1$. Experimental results of Spelt and Biesheuvel[2] show approximately 50% decrease in rise velocities of 500 $\mu$m radius bubbles with $\beta \leq 1$. Experiments by Poorte and Biesheuvel[3] for 340 and 570 $\mu$m radius bubbles with $0.0066 \leq \beta \leq 0.443$, show reductions in rise velocities of up to 35%.

We note, however, in both our simulation and in experimental data, that suppression trends with $\beta$ are not consistent. Specifically, for a given size bubble, the amount of rise suppression increases as $\beta$ increases. On the other hand, for a fixed turbulence level, the fraction of rise suppression decreases as radius decreases (and as $\beta$ increases).

There is wide agreement in the literature (Sene *et al.*[29]; Wang and Maxey[1]; Maxey *et al.*[30]; Spelt and Biesheuvel[2]) that the primary mechanism for reduction of bubble rise velocities is vortex capture, or the preferential accumulation of bubbles in regions of either low pressure or high vorticity. The general process is rising bubbles encountering and then becoming trapped inside a vortex, moving inside the vortex for a period, and then finally escaping the vortex as the latter weakens or disintegrates. Using conditional probability distributions of enstrophy $\tilde{\boldsymbol{\omega}}\tilde{\boldsymbol{\omega}}$, Wang and Maxey[1] further show that the bubbles most likely accumulate in regions of both low pressure and high vorticity.

In addition to vortex capture, Mazzitelli and Lohse[31] and Mazzitelli *et al*[32] also show that microbubbles tend to preferentially accumulate in the down-flow regions of vortices, and that this process, which further reduces the mean rise velocity, is strongly affected by the lift force experienced by the bubbles. We observe similar behavior below.

### 3.2.2 Impact of Lift Force on Suppression of Rise Velocities

To evaluate the importance of the lift force in the suppression of rise velocity, calculations with lift, $C_L = 0.59 \left( \frac{\tilde{a}\|\tilde{\boldsymbol{\omega}}\|}{\|\tilde{\boldsymbol{U}}_r\|} \right)^{1/4}$, and zero lift, $C_L = 0.0$, have been performed.

Similar analysis has been recently performed by Mazzitelli *et al*[32], though this analysis focuses on surfactant-free bubbles with $Re_b$ of order one, $C_D = 16/Re_b$ and $C_L = 1/2$. The present analysis, on the other hand, considers surfactant-contaminated bubbles, with experimental correlations of the drag and lift coefficients and $Re_b$ up to approximately 500.

Comparison of the bubble rise velocities for all four turbulent fields with lift and zero lift shows the importance of the lift force in the suppression of bubble rise velocity. As shown in Table 3 and Figure 2, the bubbles rise faster when the lift force is ignored, but the corresponding turbulent rise velocity still remains smaller than the quiescent rise velocity. As the turbulence level increases, the difference between the experimental and zero-lift cases cases becomes larger.

The mechanism by which fluctuating lift forces preferentially move bubbles to the down-flow sides of turbulent eddies has been discussed by Spelt and Biesheuvel[2] and Mazzitelli *et al.*[32]. Figure 3 shows our data for the mean vertical fluid velocities seen by bubbles as a function of bubble radius. Consistent with Spelt and Biesheuvel[2] and Mazzitelli *et al.*[32], Figure 3 shows that larger bubbles, on average, experience larger negative vertical fluid velocity. Further, Figure 4 shows that, for field 4, with $C_L = 0$ the bubbles see noticeably smaller mean downward mean velocity than is the case when the lift force is accounted for. Similar results are obtained for fields 1-3. In all cases, the mean vertical flow velocity seen by the bubbles is close to 0 when $C_L = 0$, and is significantly negative when using the experimental $C_L$. These results provide direct evidence of the contribution of lift force to moving bubbles to the down-flow sides of turbulent eddies.

## 3.3 Statistical Analysis of Rise Phenomenon

Statistical analysis of the data collected along the Lagrangian bubble paths is performed in this section. Probability distribution functions (pdfs) are computed of the bubble and local flow velocities, bubble Reynolds numbers, local vorticity, as well as bubble drag and lift forces. Where appropriate, differences between pdfs generated from simulations with $C_L = 0$ are contrasted with corresponding results using the experimental $C_L$.

### 3.3.1 Statistics of Normalized Bubble Velocity

Figure 5 shows pdfs of the normalized bubble horizontal or transverse velocity for 40 $\mu$m and 400 $\mu$m bubbles in field 1. In both cases, the pdfs are centered around 0, symmetric and nearly Gaussian. Similar pdfs, not shown, were obtained for fields 2-4. These results are consistent with the experimental data of Poorte and Biesheuvel[3]. Note that the pdfs for 400 $\mu$m bubbles are wider

than the pdfs of the 40 $\mu$m bubbles. This increase in the variance of the transverse bubble velocity with the bubble radius is consistent with the findings of section 3.2, where the mean rise velocity of large bubbles is found to be more sensitive to turbulence then it is with small bubbles.

Figures 6 and 7 show pdfs of the normalized bubble vertical velocity for fields 1-4. With the experimental $C_L$, high turbulence field 2 and lowest turbulence field 4 exhibit an asymmetry with the maximum of the pdf at a lower velocity than the mean. We shall simply qualify this type of asymmetric pdf as "negatively skewed." Conversely, we shall call "positively skewed" a pdf in which the most likely value is greater than the mean. In fields 2 and 4, the pdfs are negatively skewed when the experimental $C_L$ is used, but positively skewed when $C_L$ is set to 0. In field 3, the pdfs for 400 $\mu$m remain essentially the same when the lift force is ignored; on the other hand, by setting $C_L$ to 0, the pdf of 40 $\mu$m bubbles changes from positively skewed (experimental $C_L$) to negatively skewed ($C_L = 0$). For field 1, the pdfs are positively skewed when the experimental $C_L$ is used, but are nearly symmetric with $C_L = 0$.

Positively skewed and negatively skewed pdfs of vertical bubble velocity have been reported in prior computational studies by Spelt and Biesheuvel[2] and in experimental data of Poorte and Biesheuvel[3]. Both studies note that the departure from symmetric distributions depends upon the values of non-dimensional turbulence intensity $\beta$, and non-dimensional Taylor lengthscale $\lambda^*$. The non-dimensional Taylor lengthscale is given by $\lambda^* = \frac{\tilde{\lambda}}{\tau_b V_T} = \frac{2\tilde{\lambda}\tilde{g}}{{V_T}^2}$ where $\tilde{\lambda}$ is the dimensional Taylor length-scale and $\tau_b = \frac{V_T}{2\tilde{g}}$ is the bubble relaxation time. Spelt and Biesheuvel[2] discuss that the different observations of negative or positive "bias" of vertical velocity pdfs may result from accumulation of bubbles in "down flow regions, where their velocity is significantly reduced," versus accumulation in "downwards flowing eddies of vortices."

Figure 8 compares the computed pdf of the bubble vertical velocity for 570 $\mu$m bubbles in field 3 ($\beta = 0.17$ and $\lambda^* = 0.72$) with the experimental pdf of Poorte and Biesheuvel[3] for 570 $\mu$m bubbles with $\beta = 0.21$ and $\lambda^* = 0.54$ (their figure 9b). The computed and experimental pdfs have similar structure and are positively-skewed. Thus, the present findings are consistent with the experimental predictions of Poorte and Biesheuvel[3]. Similar observation is also made when comparing pdfs that are negatively skewed. An example is shown in Figure 9, which provides the computed pdf of the bubble vertical velocity for 400 $\mu$m bubbles in field 2 ($\beta = 0.60$ and $\lambda^* = 3.99$) and depicts the experimental data of Poorte and Biesheuvel[3] for 340 $\mu$m bubbles with $\beta = 0.44$ and $\lambda^* = 3.56$ (their figure 10b); both the computed and experimental pdfs are slightly negatively skewed.

Analysis of computed data from all parameters considered indicates that the "bias" of the bubble vertical velocity pdf toward positive or negative values has an apparently complex dependence upon $\beta$ and $\lambda^*$. Additional investigation is necessary to determine how these (and possibly other) parameters impact the nature of asymmetry of bubble vertical velocity pdfs as turbulence level changes.

### 3.3.2 Statistics of Local Flow

Pdfs of the local fluid velocities seen by the bubbles along their paths have been obtained for all parameters considered in the analysis. In all cases, results have been obtained using the experimental $C_L$ and $C_L = 0$. Results indicated that pdfs of the local transverse velocity seen by the bubbles are nearly Gaussian, and revealed insignificant differences between predictions obtained using the experimental lift and no-lift cases. On the other hand, the data show that pdfs of the local vertical velocity are not symmetric, but exhibit the same type of asymmetry as the pdfs of the vertical bubble velocity. For brevity, detailed discussion of these results is omitted.

### 3.3.3 Statistics of Relative Velocity

Figure 10 shows pdfs for of bubble Reynolds numbers for various bubble radii in fields 1 and 3. For field 3 (low turbulence), the pdfs are approximately symmetric, with one exception, and are very narrow. For field 1 (high turbulence), the pdfs are non-symmetric and are significantly wider than in field 3. Thus, spreading of the Reynolds number pdfs occurs as the turbulence level increases. Figure 10 shows that spikes in the pdfs occurs around $Re_b = 20$, for both field 1 and field 3. We believe that these spikes result from the abrupt transition in drag force correlations used at this Reynolds number.

Mean bubble Reynolds numbers ($\langle Re_b \rangle$) were also calculated and compared to the quiescent rise bubble Reynolds numbers, $Re_q$. These results are shown in Figure 11. For field 3, $\langle Re_b \rangle$ is slightly smaller than $Re_q$, but is slightly larger than $Re_q$ for field 1. Consistent with earlier observations, two competing mechanisms may explain this behavior. A slightly elevated $\langle Re_b \rangle$ would occur when the bubbles spend more time in down-flow regions, which results in a slightly higher relative velocity. A slightly reduced $\langle Re_b \rangle$ would occur as the turbulence reduces the mean rise velocity which leads to a reduction in relative velocity and hence in $Re_b$. Consistent with the wider $Re_b$ pdfs observed as turbulence level increases, Figure 11 also shows a corresponding increase in the maximum value of $Re_b$. A corresponding decrease in the minimum value of $Re_b$ also occurs. Similar trends are observed with fields 2 and 4 (not shown).

Comparison between experimental and zero lift cases are shown in Figure 12. For field 3, the difference between experimental and zero lift is barely discernible, while for field 1 the difference is small but noticeable. In the latter case, $\langle Re_b \rangle$ is slightly larger when the lift force is accounted for than when it is ignored. This trend is consistent with earlier observation that the lift force moves bubbles to the down-flow sides of eddies, which results in an increase in relative velocity and hence, on average, of $Re_b$. Similar results are also obtained for fields 2 and 4 (not shown).

### 3.3.4 Statistics of Vorticity

As shown in Figure 13, for field 3 (low turbulence) the pdf of vorticity seen by bubbles (of radii 20 and 600 $\mu$m) is very close to the vorticity pdf of the isotropic

turbulent field. Specifically, the mean vorticity seen by the bubbles is slightly less than the the mean vorticity of the flow. The same observation is made for field 4 (not shown).

For field 1 (high turbulence), also shown in Figure 13, analysis indicates that 10 $\mu$m bubbles see a mean vorticity slightly less than that of the flow field, and the pdf of the vorticity seen by these bubbles is slightly distorted toward lower values compared to the pdf of the field vorticity. On the other hand, the pdf of 600 $\mu$m bubbles is much broader than that of the flow, with a significantly larger mean value.

Comparison is made between the vorticity pdfs of Figure 13, the $Re_b$ pdfs of Figure 10 and the maximum, mean, minimum and quiescent rise $Re_b$ of Figure 11. In weak turbulence, the behavior of bubbles of all sizes considered is mildly affected by the turbulence; thus, the bubbles tend to sample the mean flow, and consequently the pdfs of vorticity experienced by the bubbles are nearly identical to that of the flow. When turbulence is strong, however, the behavior of tiny, 10-20 $\mu$m bubbles differs significantly from that of the larger, 600 $\mu$m bubbles. The tiny bubbles tend to behave like flow tracers, as drag dominates and slip is negligible, and consequently the pdf of vorticity experienced by these bubbles remains close to that of the flow. Larger bubbles, on the other hand, can be efficiently captured by the turbulent eddies, and thus exhibit broader pdfs of vorticity and Reynolds number.

The effect of the lift force on the vorticity seen by the bubbles is examined in Figure 14. Included in these results are predictions for fields 1 and 3; results for fields 2 and 4 show similar trends and are omitted. Figure 14 shows that when the lift force is ignored, the bubbles see on average a slightly larger vorticity. This trend is consistent with the earlier observation that the lift force tends to move bubbles preferentially to the periphery of the eddies, where they accordingly see smaller vorticity and larger downflow velocity.

### 3.3.5 Statistics of Lift Forces

From the recorded values of bubble velocity, fluid velocity and vorticity, a detailed statistical analysis was performed of the drag and lift forces experienced by the bubbles. The study of the drag forces reveal trends that closely mirror those established based on the analysis of bubble Reynolds numbers. Consequently, we focus primarily on the behavior of lift forces.

Figure 15 shows the mean total lift, $\langle L \rangle$, and drag, $\langle D \rangle$, forces for different sizes of bubbles in fields 1 and 3. As expected, for both fields 1 and 3, both the total drag and lift forces increase rapidly with bubble radius. Note, however, that mean total drag is smaller in field 1 (high turbulence) than it is in field 3 (low turbulence), whereas the opposite is true for the lift force. This trend is most evident for the larger bubble sizes. The reduction of the mean total drag with increasing turbulence is consistent with earlier observation that, within the parameter range considered, turbulence tends to suppress the bubble rise velocities and the mean slip velocities. The increasing importance of lift forces as turbulence levels increase is also expected, given the increasing tendency

of bubbles to be trapped by turbulent eddies, and consequently to experience larger vorticity.

Additional insight into the significance of the lift force can be gained from Table 4, which provides the ratio of lift to drag forces for different bubble sizes. In particular, the table indicates that in fields 2–4, the mean lift force is dominated by the mean drag, as the ratio $\langle L \rangle / \langle D \rangle$ remains below 3%. In field 1, however, the mean total lift force is more significant, reaching 15% of the total drag for the 500 $\mu$m bubbles. Thus, in the present parameter regime, the magnitude of the mean lift becomes more significant with increasing turbulence level and bubble size.

Figures 16 and 17 show pdfs of the vertical component of the lift force, $L_z$, for fields 3 and 1, respectively. In field 3 (low turbulence), the pdfs are nearly symmetric and centered when the bubble radius is 100 $\mu$m or smaller, but are asymmetric with long negative tails when the bubble size is larger. In field 1 (high turbulence), the pdfs of $L_z$ are also approximately symmetric and centered for small bubbles, namely when the radius is 120 $\mu$m or smaller. For larger bubble radii, the pdfs become asymmetric. However, unlike the pdfs in field 3, with increasing bubble radius the pdfs in field 1 develop increasingly broader positive tails.

An immediate consequence of the results in Figures 16 and 17 is that the mean vertical lift is negative in field 3, but positive in field 1. This can be verified in Table 5, which provides normalized values of the mean vertical lift in fields 1–4. As expected, weak negative mean vertical lift is observed in fields 3 and 4, but strong positive means are observed in field 1 especially at higher bubble radii. Thus, the results provide additional insight into the increasing significance of the lift force as the turbulence level and the bubble size increase.

The structure of the pdfs for $L_z$ at low and high turbulence may be explained on the basis of simplified arguments. In weak turbulence the motion of the bubbles is dominated by buoyancy forces and weakly affected by the local hydrodynamic pressure gradients. In this case, a perturbative argument based on the observation that when negative lift occurs, the vertical rise of the bubble is reduced and consequently it tends to remain in the same region associated with the negative lift event; the opposite occurs when a positive lift occurs. Meanwhile, at high turbulence, the occurrence of a positive mean vertical lift is consistent with the simplified cartoon in which the bubble is trapped in the downflow region of a (horizontal) vortex core. For this quasi-steady cartoon, the bubble is located above the vortex center, and as a result, the radial lift force has a positive vertical component.

# 4 Generalized Dispersion Analysis

## 4.1 Scale Decomposition of a Non-Fickian Process

In this section we review the fundamental concepts needed for the characterization of the scale-dependent dispersion of the bubbles in an isotropic turbulent field. The analysis follows that of Cushman and Moroni[17] and Moroni and Cushman[18], who studied the anomalous dispersion of tracer particles in a porous medium.

To start, consider the trajectory $\boldsymbol{X}(t)$ of a single particle, which is a real-valued random process defined on a suitable abstract probability space $(\Omega, \mathcal{A}, P)$. Since the bubble trajectory results from finite forcing applied by the turbulent flow, $\boldsymbol{X}(t)$ can be differentiated at least twice with respect to time. In this section, we denote by the brackets $\langle . \rangle$ the expectation induced by the probability measure $P$. It will be further assumed that $\boldsymbol{X}(t)$ and its time derivative are second-order processes, i.e.

$$\left\langle \|\boldsymbol{X}(t)\|^2 \right\rangle < \infty, \quad \left\langle \|d\boldsymbol{X}(t)/dt\|^2 \right\rangle < \infty, \quad \forall t.$$

Because the bubble dynamics are invariant to spatial and time translations, and the analysis is being performed at equilibrium, the reference to the initial position of the particle is irrelevant and only the random displacement $\Delta\boldsymbol{X}(t) = \boldsymbol{X}(t) - \boldsymbol{X}(0)$ is of interest. We denote by $G(\Delta\boldsymbol{x}, t)$ the probability density function that the particle has experienced a displacement $\Delta\boldsymbol{x}$ at time $t$ from its initial position:

$$G(\Delta\boldsymbol{x}, t) = \left\langle \delta(\Delta\boldsymbol{x} - \Delta\boldsymbol{X}(t)) \right\rangle, \tag{25}$$

where $\delta$ denotes the Dirac delta function. Since $G$ is a density,

$$\int_{\mathbb{R}^3} G(\Delta\boldsymbol{x}, t) d(\Delta\boldsymbol{x}) = 1.$$

The Fourier transform of $G$ is given by:

$$\begin{aligned} \widehat{G}(\boldsymbol{k}, t) \equiv \mathcal{F}\{G\} &= \int_{\mathbb{R}^3} e^{i\boldsymbol{k}\cdot\Delta\boldsymbol{x}} G(\Delta\boldsymbol{x}, t) d(\Delta\boldsymbol{x}) = \left\langle e^{i\boldsymbol{k}\cdot\Delta\boldsymbol{X}(t)} \right\rangle \\ &= \left\langle \cos(\boldsymbol{k}\cdot\Delta\boldsymbol{X}) \right\rangle + i \left\langle \sin(\boldsymbol{k}\cdot\Delta\boldsymbol{X}) \right\rangle. \end{aligned} \tag{26}$$

In the context of dispersion analysis, the Fourier transform of $G$ is often called the self-part of the intermediate scattering function. In probability theory, $\widehat{G}(\boldsymbol{k}, \cdot)$ is the characteristic function of the $\mathbb{R}^3$-valued random variable $\Delta\boldsymbol{X}(\cdot)$ (indexed on time). Provided that $\langle |\Delta\boldsymbol{X}(t)|^m \rangle < \infty$ for some integer $m > 0$, $\widehat{G}$ has continuous partial derivatives up to order $m$, and

$$\frac{\partial^m}{\partial k_{j_1} \dots \partial k_{j_m}} \widehat{G}(\boldsymbol{k}, t) = i^m \left\langle \Delta X_{j_1}(t) \dots \Delta X_{j_m}(t) e^{i\boldsymbol{k}\cdot\Delta\boldsymbol{X}(t)} \right\rangle. \tag{27}$$

Let us now decompose the random displacement in terms of its mean and fluctuating parts: $\Delta \boldsymbol{X}(t) = \langle \Delta \boldsymbol{X} \rangle (t) + \Delta \boldsymbol{X}'(t)$. Then, from (26) it follows that

$$\widehat{G}(\boldsymbol{k}, t) = e^{i\boldsymbol{k} \cdot \langle \Delta \boldsymbol{X} \rangle (t)} \left\langle e^{i\boldsymbol{k} \cdot \Delta \boldsymbol{X}'(t)} \right\rangle = e^{i\boldsymbol{k} \cdot \langle \Delta \boldsymbol{X} \rangle (t)} \widehat{G}'(\boldsymbol{k}, t). \tag{28}$$

Differentiating with respect to time, one obtains:

$$\frac{\partial \widehat{G}(\boldsymbol{k}, t)}{\partial t} = i(\boldsymbol{k} \cdot \overline{\boldsymbol{v}}) \widehat{G}(\boldsymbol{k}, t) + e^{i\boldsymbol{k} \cdot \langle \Delta \boldsymbol{X} \rangle (t)} \frac{\partial \widehat{G}'(\boldsymbol{k}, t)}{\partial t}. \tag{29}$$

where $\overline{\boldsymbol{v}}$ is used to denote the expected velocity $d \langle \Delta \boldsymbol{X} \rangle / dt = d \langle \boldsymbol{X}(t) \rangle / dt$, which is time independent. We assume that $\widehat{G}$ is sufficiently well-behaved to satisfy the following integral equation

$$\frac{\partial \widehat{G}'(\boldsymbol{k}, t)}{\partial t} = -\int_0^t \widehat{K}'(\boldsymbol{k}, \tau) \widehat{G}'(\boldsymbol{k}, t - \tau) + \frac{\partial \widehat{G}'}{\partial t}(\boldsymbol{k}, 0). \tag{30}$$

where $\widehat{K}'$ is a dispersion kernel. Noting that $\partial \widehat{G}'/\partial t = 0$ at $t = 0$, (29) becomes

$$\begin{aligned} \frac{\partial \widehat{G}(\boldsymbol{k}, t)}{\partial t} &= i(\boldsymbol{k} \cdot \overline{\boldsymbol{v}}) \widehat{G}(\boldsymbol{k}, t) - \int_0^t e^{i\boldsymbol{k} \cdot \langle \Delta \boldsymbol{X} \rangle (t)} \widehat{K}'(\boldsymbol{k}, \tau) \widehat{G}'(\boldsymbol{k}, t - \tau) \\ &= i(\boldsymbol{k} \cdot \overline{\boldsymbol{v}}) \widehat{G}(\boldsymbol{k}, t) - \int_0^t \Delta(\boldsymbol{k}, \tau) \widehat{K}'(\boldsymbol{k}, \tau) \widehat{G}(\boldsymbol{k}, t - \tau), \end{aligned} \tag{31}$$

where

$$\Delta(\boldsymbol{k}, \tau) = e^{i\boldsymbol{k} \cdot [\langle \Delta \boldsymbol{X} \rangle (t) - \langle \Delta \boldsymbol{X} \rangle (t - \tau)]} \tag{32}$$

is time independent by virtue of the time invariance of the dynamics. To determine the dispersion kernel, $\widehat{K}'$, we introduce the Laplace transform (in time),

$$\widetilde{f}(s) = \int_0^\infty f(\tau) e^{-s\tau} d\tau, \tag{33}$$

and from (30) we obtain

$$\widetilde{\widehat{K}'}(\boldsymbol{k}, s) = -\frac{\widetilde{\partial^2 \widehat{G}'/\partial t^2}}{s \widetilde{\widehat{G}}'}. \tag{34}$$

Differentiating the self-part of the intermediate scattering function twice in time, one obtains

$$\frac{\partial^2 \widehat{G}'}{\partial t^2} = i\boldsymbol{k} \cdot \left\langle \boldsymbol{a}'(t) e^{i\boldsymbol{k} \cdot \Delta \boldsymbol{X}'(t)} \right\rangle + i\boldsymbol{k} \cdot \left\langle \boldsymbol{v}'(t) e^{i\boldsymbol{k} \cdot \Delta \boldsymbol{X}'(t)} \boldsymbol{v}'(t) \right\rangle \cdot (i\boldsymbol{k}), \tag{35}$$

where $\boldsymbol{v}'(t)$ and $\boldsymbol{a}'(t)$ are the fluctuating velocity and acceleration of the bubble, respectively. This shows that the Laplace transform of the kernel splits into two components,

$$\widetilde{\widehat{K}'} = i\boldsymbol{k} \cdot \widetilde{\widehat{\boldsymbol{D}}'}_1 + i\boldsymbol{k} \cdot \widetilde{\widehat{\boldsymbol{D}}'}_2 \cdot i\boldsymbol{k}, \tag{36}$$

with

$$\widetilde{\widehat{\boldsymbol{D}}'}_1 = \frac{\left\langle \boldsymbol{a}'(t)\widetilde{e^{i\boldsymbol{k}\cdot\Delta\boldsymbol{X}'(t)}}\right\rangle}{\widetilde{s\widehat{G}'}}, \quad \widetilde{\widehat{\boldsymbol{D}}'}_2 = \frac{\left\langle \boldsymbol{v}'(t)\widetilde{e^{i\boldsymbol{k}\cdot\Delta\boldsymbol{X}'(t)}}\boldsymbol{v}'(t)\right\rangle}{\widetilde{s\widehat{G}'}}. \tag{37}$$

Due to the linearity of the Laplace transform, the split kernel can be inserted into (31). Next, by applying an inverse Fourier transform we obtain the following governing equation for the displacement density:

$$\begin{aligned} &\frac{\partial G(\Delta\boldsymbol{x},t)}{\partial t} = -\boldsymbol{\nabla}_{\Delta\boldsymbol{x}}\cdot[\overline{\boldsymbol{v}}G(\Delta\boldsymbol{x},t)] \\ + \quad &\boldsymbol{\nabla}_{\Delta\boldsymbol{x}}\cdot\int_0^t\int_{\mathbb{R}^3}\boldsymbol{D}_1(\Delta\boldsymbol{y},\tau)G(\Delta\boldsymbol{x}-\Delta\boldsymbol{y},t-\tau)d\Delta\boldsymbol{y}d\tau \\ + \quad &\boldsymbol{\nabla}_{\Delta\boldsymbol{x}}\cdot\int_0^t\int_{\mathbb{R}^3}\boldsymbol{D}_2(\Delta\boldsymbol{y},\tau)\cdot\boldsymbol{\nabla}_{\Delta\boldsymbol{x}-\Delta\boldsymbol{y}}G(\Delta\boldsymbol{x}-\Delta\boldsymbol{y},t-\tau)d\Delta\boldsymbol{y}d\tau \end{aligned} \tag{38}$$

Equation (38) is the general form of a convection dispersion process, involving both time and space convolutions. It is, however, of little interest since we are more concerned by the scale-dependent dispersion properties, as characterized by the tensors $\widehat{\boldsymbol{D}}_1 = \Delta\widehat{\boldsymbol{D}}'_1$ and $\widehat{\boldsymbol{D}}_2 = \Delta\widehat{\boldsymbol{D}}'_2$. Computation of these tensors from (37) in Laplace space is too cumbersome. An alternative computational approach, based on (30), is presented in section 4.3 below.

## 4.2 Small wave-vector approximation

In this section, we focus on the small wave-vector limit $\|\boldsymbol{k}\| << 1$ of the expressions for scale-dependent dispersion. Taking the Laplace transform of (31), we have:

$$s\widetilde{\widehat{G}}(\boldsymbol{k},s) - \widehat{G}(\boldsymbol{k},0) = i(\boldsymbol{k}\cdot\overline{\boldsymbol{v}})\widetilde{\widehat{G}}(\boldsymbol{k},s) - \widetilde{\widehat{K}}(\boldsymbol{k},s)\widetilde{\widehat{G}}(\boldsymbol{k},s), \tag{39}$$

where $\widehat{K}(\boldsymbol{k},\tau) = \widehat{K}'(\boldsymbol{k},\tau)\Delta(\boldsymbol{k},\tau)$. Since $G(\Delta\boldsymbol{x},0) = \delta(\Delta\boldsymbol{x})$, *i.e.* the displacement at the initial time is almost surely zero, $\widehat{G}(\boldsymbol{k},0) = 1$, $\forall\boldsymbol{k}$; inserting this last expression into (39) results in:

$$\widetilde{\widehat{G}}(\boldsymbol{k},s) = \left[s - i\boldsymbol{k}\cdot\overline{\boldsymbol{v}} + \widetilde{\widehat{K}}(\boldsymbol{k},s)\right]^{-1}. \tag{40}$$

The Taylor expansion of $\widehat{G}(\boldsymbol{k},t)$ from (26) around $\|\boldsymbol{k}\| \equiv k = 0$ is

$$\widehat{G}(\boldsymbol{k},t) = 1 + i\boldsymbol{k}\left\langle\Delta\boldsymbol{X}(t)\right\rangle - \frac{1}{2}\boldsymbol{k}\cdot\left\langle\Delta\boldsymbol{X}(t)\Delta\boldsymbol{X}(t)\right\rangle\cdot\boldsymbol{k} + O(k^3). \tag{41}$$

Using $\left\langle\Delta\boldsymbol{X}(t)\right\rangle = \overline{\boldsymbol{v}}t$, the Laplace transform of the Taylor expansion of $\widehat{G}$ is

$$\widetilde{\widehat{G}}(\boldsymbol{k},s) = s^{-1} + i\boldsymbol{k}\cdot\overline{\boldsymbol{v}}s^{-2} - \frac{1}{2}\boldsymbol{k}\cdot\widetilde{\left\langle\Delta\boldsymbol{X}(t)\Delta\boldsymbol{X}(t)\right\rangle}\cdot\boldsymbol{k} + O(k^3). \tag{42}$$

From (40) and (42) we find to leading order the expression of the Laplace transform of the kernel $\widehat{K}$:

$$\widetilde{\widehat{K}}(\boldsymbol{k},s)=\boldsymbol{k}\cdot\left[(\overline{\boldsymbol{vv}})s^{-1}-\frac{1}{2}\widetilde{\langle\Delta\boldsymbol{X}(t)\Delta\boldsymbol{X}}(t)\rangle s^2\right]\cdot\boldsymbol{k},\quad k<<1. \tag{43}$$

Comparison with (36) shows that in the limit of $k\to 0$, $\widehat{\boldsymbol{D}}_1=0$ and

$$\widetilde{\widehat{\boldsymbol{D}}}_2=\frac{-\overline{\boldsymbol{vv}}}{s}+\frac{\widetilde{\langle\Delta\boldsymbol{X}(t)\Delta\boldsymbol{X}}(t)\rangle}{2}s^2. \tag{44}$$

It should be noted that in the limit of small wave-vector, the generalized dispersion tensor $\widehat{\boldsymbol{D}}_2$ is scale independent. In the following, the small wave-vector approximation of $\widehat{\boldsymbol{D}}_2$ is denoted $\widehat{\boldsymbol{D}}_{k\downarrow 0}$. Also, using the properties of the Laplace transform, and that at $t=0$ $\langle\Delta\boldsymbol{X}\Delta\boldsymbol{X}\rangle=0$ together with its time derivative, we have:

$$s^2\widetilde{\langle\Delta\boldsymbol{X}\Delta\boldsymbol{X}}\rangle=\left(\frac{d^2\,\widetilde{\langle\Delta\boldsymbol{X}\Delta\boldsymbol{X}}\rangle}{dt^2}\right)$$

which is used to convert (44) to the time domain according to:

$$\frac{d^2\,\langle\Delta\boldsymbol{X}\Delta\boldsymbol{X}\rangle}{dt^2}=2\overline{\boldsymbol{vv}}+2\widehat{\boldsymbol{D}}_{k\downarrow 0}(t). \tag{45}$$

Integrating the last equation once we have:

$$\frac{d\,\langle\Delta\boldsymbol{X}\Delta\boldsymbol{X}\rangle}{dt}=2\left[\overline{\boldsymbol{vv}}t+\int_0^t\widehat{\boldsymbol{D}}_{k\downarrow 0}(\tau)d\tau\right]. \tag{46}$$

where $\langle\Delta\boldsymbol{X}\Delta\boldsymbol{X}\rangle$ represents the second moment of displacement.

On the other hand, differentiating $\langle\Delta\boldsymbol{X}\Delta\boldsymbol{X}\rangle$ with respect to time and using stationarity of the dynamics also yields

$$\begin{aligned}\frac{1}{2}\frac{d\,\langle\Delta\boldsymbol{X}\Delta\boldsymbol{X}\rangle}{dt} &= \langle\Delta\boldsymbol{X}(t)\boldsymbol{v}(t)\rangle=\left\langle\boldsymbol{v}(t)\int_0^t\boldsymbol{v}(\tau)\mathrm{d}\tau\right\rangle=\int_0^t\langle\boldsymbol{v}(t)\boldsymbol{v}(\tau)\rangle\,d\tau\\ &= \overline{\boldsymbol{vv}}t+\int_0^t\langle\boldsymbol{v}'(t)\boldsymbol{v}'(\tau)\rangle\,d\tau=\overline{\boldsymbol{vv}}t+\int_0^t\langle\boldsymbol{v}'(t)\boldsymbol{v}'(t+\tau)\rangle\,d\tau\end{aligned} \tag{47}$$

Comparing (46) with (47), one deduces that

$$\widehat{\boldsymbol{D}}_{k\downarrow 0}(\tau)=\langle\boldsymbol{v}'(t)\boldsymbol{v}'(t+\tau)\rangle\,, \tag{48}$$

which is in agreement with Taylor's theory [33;34] where the Lagrangian fluid velocity is replaced by the Lagrangian bubble velocity. In other words, the expected velocity and its two-times correlations are all that are needed to characterize the evolution of the tensor of second moments of displacements.

### 4.3 Implementation

We now consider the application of the theory above to the analysis of bubble dispersion in turbulence. It is first remarked that the turbulent fields used in this study are homogeneous and stationary; accordingly, the bubbles are subjected to external forces that are isotropic in the transverse plane ($x$ and $y$) and homogeneous along the longitudinal (also vertical or $z$) direction. As a result, the expected displacement $\langle \Delta \boldsymbol{X}(t) \rangle$ and its (constant) time derivative $\overline{\boldsymbol{v}}$ have only one non-zero component along the homogeneous $z$ direction, and the dispersion tensor is diagonal, allowing for separate analysis along the transverse and longitudinal directions. In the following we use subscripts $t$ and $l$ to distinguish between transverse and longitudinal components respectively. We also denote $\mathbf{1}_t$ and $\mathbf{1}_l$ as unit vectors in the transverse and longitudinal directions respectively.

Empirical estimates of the expectations appearing in the various equations to be solved are based on the available sample set of bubble trajectories, with all bubbles having the same radius and being in the same turbulent field. For instance, the self-parts of the intermediate scattering functions are estimated by

$$\widehat{G}_{t,l}(k,t) = \left\langle e^{ik\mathbf{1}_{t,l} \cdot \Delta \boldsymbol{X}(t)} \right\rangle \approx \frac{1}{N} \sum_{i=1}^{N} e^{ik\mathbf{1}_{t,l} \cdot \Delta \boldsymbol{x}_i(t)}, \tag{49}$$

where $k$ is the (scalar) wavenumber, $\Delta \boldsymbol{x}_i(t) = \boldsymbol{x}_i(t) - \boldsymbol{x}_i(0)$ and $\{\boldsymbol{x}_i(t), i = 1, \ldots, N\}$ is the sample set of trajectories. Similarly, we denote $\{\boldsymbol{v}_i(t), i = 1, \ldots, N\}$ as the sample set of the bubbles' instantaneous Lagrangian velocities. The self-parts of the intermediate scattering functions satisfy:

$$\frac{\partial \widehat{G}_{t,l}}{\partial t}(k,t) = ik\mathbf{1}_{t,l} \cdot \overline{\boldsymbol{v}} \widehat{G}_{t,l}(k,t) - \int_0^t \widehat{K}_{t,l}(k,\tau) \widehat{G}_{t,l}(k,t-\tau) d\tau.$$

Note that the first term on the right-hand side of the equation above vanishes for the transverse direction as $\overline{\boldsymbol{v}} \cdot \mathbf{1}_t = 0$. Differentiating in time and rearranging terms yields the kernel equation:

$$\widehat{K}_{t,l}(k,t) = -\frac{\partial \widehat{G}_{t,l}(k,t)}{\partial t^2} + ik\mathbf{1}_{t,l} \cdot \overline{\boldsymbol{v}} \frac{\partial \widehat{G}_{t,l}(k,t)}{\partial t} - \int_0^t \widehat{K}_{t,l}(k,\tau) \frac{\partial \widehat{G}_{t,l}(k,t)}{\partial \tau} d\tau. \tag{50}$$

This kernel equation is solved for $t \in [0, T]$ through a time integration procedure. Let us define the time-step $\Delta t = T/n$ such that $t_j = j\Delta t$. The sample set estimate of $\widehat{G}_{t,l}$ is first computed for a given wavenumber $k$ at times $t_j$, $j = 0, \ldots, n$, using (49). To simplify the notation, we suppress the explicit dependence on $k$ in the expressions below. The estimate of first and second time-derivatives of $\widehat{G}$, respectively denoted $\dot{\widehat{G}}$ and $\ddot{\widehat{G}}$, are computed at the discrete times $t_j$; at the initial time $t_j = 0$ we use the exact expressions,

$$\dot{\widehat{G}}_{t,l}(0) = ik\mathbf{1}_{t,l} \cdot \overline{\boldsymbol{v}}, \tag{51}$$

$$\ddot{\widehat{G}}_{t,l}(0) = -(k\mathbf{1}_{t,l}) \cdot \overline{\boldsymbol{v}\boldsymbol{v}} \cdot (k\mathbf{1}_{t,l}), \tag{52}$$

where the mean velocity vector $\overline{\boldsymbol{v}}$ and second moment velocity tensor $\overline{\boldsymbol{vv}}$ are taken as sample estimate values:

$$\overline{\boldsymbol{v}} \approx \frac{1}{Nn}\sum_{i=1}^{N}\sum_{j=0}^{n}\boldsymbol{v}_i(t_j), \quad \overline{\boldsymbol{vv}} \approx \frac{1}{Nn}\sum_{i=1}^{N}\sum_{j=0}^{n}\boldsymbol{v}_i(t_j)\boldsymbol{v}_i(t_j).$$

At intermediate discrete times, the derivatives of $\widehat{G}$ are estimated using standard, second-order, centered differences; for $j = 1, \ldots, n-1$,

$$\dot{\widehat{G}}_{t,l}(t_j) = \frac{\widehat{G}_{t,l}(t_{j+1}) - \widehat{G}_{t,l}(t_{j-1})}{2\Delta t}, \tag{53}$$

$$\ddot{\widehat{G}}_{t,l}(t_j) = \frac{\widehat{G}_{t,l}(t_{j+1}) - 2\widehat{G}_{t,l}(t_j) + \widehat{G}_{t,l}(t_{j-1})}{\Delta t^2}. \tag{54}$$

At $t_n = T$, the following one-sided, second-order approximations are used:

$$\dot{\widehat{G}}_{t,l}(t_n) = \frac{3\widehat{G}_{t,l}(t_n) - 4\widehat{G}_{t,l}(t_n - 1) + \widehat{G}_{t,l}(t_n - 2)}{\Delta t}, \tag{55}$$

$$\ddot{\widehat{G}}_{t,l}(t_n) = \frac{2\widehat{G}_{t,l}(t_n) - 5\widehat{G}_{t,l}(t_n - 1) + 4\widehat{G}_{t,l}(t_n - 2) - \widehat{G}_{t,l}(t_n - 3)}{\Delta t^2}. \tag{56}$$

We now proceed with the discrete resolution of the kernel equation (50) using a time stepping scheme, using the starting value

$$\widehat{K}_{t,l}(t = 0) = -\ddot{\widehat{G}}_{t,l}(0) + ik\mathbf{1}_{t,l} \cdot \overline{\boldsymbol{v}}\dot{\widehat{G}}_{t,l}(0).$$

Assuming that the kernel values have been computed at the discrete times $t_i$, $0 \le i \le m$, then the kernel value at time $t_{m+1}$ satisfies the linear equation

$$\begin{aligned}\widehat{K}_{t,l}(t_{m+1}) &= -\ddot{\widehat{G}}_{t,l}(t_{m+1}) + ik\mathbf{1}_{t,l} \cdot \overline{\boldsymbol{v}}\dot{\widehat{G}}_{t,l}(t_{m+1}) \\ &- \frac{\Delta t}{2}\widehat{K}_{t,l}(t_0)\widehat{G}_{t,l}(t_{m+1}) + \frac{\Delta t}{2}\widehat{K}_{t,l}(t_{m+1})\widehat{G}_{t,l}(t_0) \\ &+ \Delta t\sum_{j=1}^{m}\widehat{K}_{t,l}(t_j)\widehat{G}_{t,l}(t_{m+1-j}),\end{aligned} \tag{57}$$

where the convolution has been approximated using Simpson's rule. The generalized dispersion coefficients $\widehat{D}(k, \tau)$ are then deduced from

$$\widehat{\boldsymbol{D}}_{t,l}(k, \tau) = \widehat{K}_{t,l}(k, \tau)/k^2.$$

We note that both $\widehat{\boldsymbol{D}}_t(k, \tau)$ and $\widehat{\boldsymbol{D}}_l(k, \tau)$ must decay to 0 for all wavenumbers $k$ in order for the dispersion process to transition to Fickian.

## 4.4 Detailed analysis for 400 $\mu$m bubbles in Field 2

To illustrate the methodology outlined above, we show a detailed step-by-step analysis of the dispersion of 400 $\mu$m bubbles in field 2. The sample set consists

of the trajectories and velocities of 5,000 bubbles, recorded every $\Delta t = 0.1$ over a time span of $T_r = 200$. In order to provide a graphical illustration of the dispersion of the bubbles in the turbulence, we plot in Figure 18 the trajectories of 100 bubbles over the time span of the analysis.

The self-part of the intermediate scattering function in the transverse and longitudinal directions, respectively $\widehat{G}_t$ and $\widehat{G}_l$, are estimated using (49). To improve the statistical convergence of the estimates, different initial positions along the bubbles trajectories are considered. Indeed, provided that the initial positions along a bubble trajectory are taken at time intervals greater than the integral time-scale of the flow, the displacement from these initial positions may be considered as statistically independent. Figure 19 shows the resulting sample-based estimates of the real and imaginary parts of $\widehat{G}_t(k,t)$. Since $\widehat{G}_t$ is the Fourier transform of the transverse displacement pdf, and since the turbulence is isotropic in the transverse plane, the imaginary part is expected to be zero by symmetry (negative and positive displacements of same magnitude are equally likely). This is verified in Figure 19 where $Im(\widehat{G}_t)$ takes only small values (compared to the real part), which can be attributed to sampling errors. Since the average velocity in the transverse direction is zero, $Re(\widehat{G}_t)$ can be interpreted as the probability that the bubbles remain in a neighborhood of size $2\pi/k$ of their initial positions after a time lag $\tau$. Figure 19 shows that as $k$ increases, *i.e.* as the extent of the neighborhood shrinks to zero, the probability that bubbles remain in the corresponding neighborhood goes to zero in shorter and shorter time scales.

Figure 20 shows the real and imaginary parts of $\widehat{G}_l$. Along this direction the bubbles have a non-zero average velocity, and the displacement pdf in the longitudinal direction is no longer expected to be centered or symmetric. As a result, the imaginary part of $\widehat{G}_l$ takes significant positive values, denoting a positive mean displacement. However, for given wavenumber $k > 0$, the magnitude $|\widehat{G}_l|$ goes to zero as time increases. Again, the increasing decay rate of $|\widehat{G}_l|$ with time, for increasing $k$, denotes a faster decay of the probability that bubbles remain in a neighborhood with characteristic size $2\pi/k$ around their initial position.

The dispersion kernels $\widehat{K}_{t,l}$ are then computed, as discussed in section 4.3, to obtain the generalized dispersion coefficients $\widehat{\boldsymbol{D}}_{t,l}(k,\tau)$. The real part of the generalized dispersion coefficient in the transverse direction is shown in Figure 21. The imaginary part of $\widehat{\boldsymbol{D}}_t$, not shown, is negligible compared to the real part and is due to sampling errors. Figure 21 shows that $\widehat{\boldsymbol{D}}_t$ is weakly dependent on $k$ over the range of wavenumbers analyzed, but exhibits a slightly higher decay rate as $k$ increases. The plot also demonstrates the non-Fickian character of the transverse dispersion process, as non-trivial variation of $D$ is observed for all length scales.

In order to verify the numerical predictions of the generalized dispersion coefficients, we compare the computed values of $\widehat{\boldsymbol{D}}_t$ for small wavenumbers with independent asymptotic estimates. As discussed in section 4.2, in the limit $k \to 0$, $\widehat{\boldsymbol{D}}_t$ tends to the two-times velocity correlation function. For the

present case, the latter is shown in Figure 22. Comparison of Figures 21 and 22 shows that there is a close agreement between the two estimates, which provides confidence in the numerical procedure for estimating the dispersion coefficients.

The real and imaginary part of the generalized dispersion coefficient in the longitudinal direction are shown in Figure 23. Here, the dependence of $\widehat{\boldsymbol{D}}_l$ on the wavenumber is much more important, with the decay timescale of $\widehat{\boldsymbol{D}}_l$ increasing significantly as $k$ increases. Thus, large scales take longer times than small scales to reach the Fickian regime. Also, comparison with Figure 21 shows that dispersion in the longitudinal direction takes a longer time than in the transverse to approach a Fickian process. This can also be observed in Figure 22 by comparing the decay rates of the velocity correlations in the transverse and longitudinal directions.

In order to further verify the predictions, and to make a connection with classical Fickian analyses, we examine in Figure 24 the time evolution of the variances of the displacement, $\left\langle \Delta \boldsymbol{X}'(\tau)^2 \right\rangle$, in the transverse and longitudinal directions. The linear asymptotic behavior (at large times) predicted by the analysis is verified. Specifically, the displacement curves show that the variances increase linearly after time lags $\tau \simeq 0.2$ and 0.3 in the transverse and longitudinal directions respectively. In addition, there is a fairly good agreement between the asymptotic slopes of displacement curves and the same slopes predicted from the integration of the generalized dispersion coefficients computed for a small wavenumber, $k = 0.1$; see (46). This agreement provides additional confidence in the predictions, and illustrates how generalized and Fickian dispersion analyses can be connected when appropriate.

## 4.5 Effect of Bubble Radius and Turbulence Intensity

The generalized dispersion analysis has been performed for all 4 turbulent fields, and for bubbles with radius 40 and 400 $\mu$m.

Figure 25 shows the real and imaginary parts of the generalized dispersion coefficient in the longitudinal direction for 40 $\mu$m bubbles and fields 1-4. It can be seen that the main impact of the turbulence is to decrease the decay timescale of $\widehat{\boldsymbol{D}}_l$. Specifically, it takes roughly 0.1 second for $\widehat{\boldsymbol{D}}_l$ to go to zero in field 1, while a time lag of more than 10 seconds is necessary to reach the Fickian regime in field 4. Similar results are found for the analysis of the displacement in the transverse direction (not shown). These observations imply that the trajectories of the bubbles remain correlated over a longer time period as the turbulence level decreases with as a result anomalous dispersion over longer (dimensional) time scales. Additional insight into the correlation decay can be gained from Figure 26, where the evolution of the two-time velocity correlations in the transverse and longitudinal directions is plotted in terms of the normalized time lag. One can observe that for these bubbles the decay time scale is weakly dependent on the turbulence intensity. By virtue of normalization conventions, one consequently concludes that, for the 40 $\mu$m bubbles, the transition from anomalous to Fickian diffusion occurs over time periods that scales with the turbulence integral time scale, for the entire range of dissipation rates considered

in the analysis.

Figure 27 shows the real and imaginary parts of the generalized dispersion coefficient in the longitudinal direction for the 400 $\mu$m bubbles in fields 1-4. It shows that for the two-highest turbulence levels (fields 1 and 2), $\widehat{\boldsymbol{D}}_l$ has qualitatively the same behavior as for the 40 $\mu$m bubbles. However, the longitudinal generalized dispersion coefficients have larger value for the larger bubbles, but decay at a slightly higher rate.

Contrary to the results for fields 1 and 2, the generalized dispersion coefficient for 400 $\mu$m bubbles in the longitudinal direction for fields 3 and 4 exhibits a qualitatively different behavior than that of the 40 $\mu$m bubbles. Specifically, the decay of the real and imaginary parts of $\widehat{\boldsymbol{D}}$ exhibit large oscillations and significant negative values, even for the smallest wavenumbers analyzed. Fickian behavior is evidently not approached within the time span depicted.

The oscillations in $\widehat{\boldsymbol{D}}_l$ for fields 3 and 4 in Figure 27 appear to be related to the "crossing trajectory effect." As discussed by Yudine[35], Corrsin[36], Snyder and Lumley[19] and Mazzitelli and Lohse[20], this phenomenon occurs when, due to buoyancy effects, bubbles rapidly leave flow regions where the velocity is highly correlated and enter regions where flow velocities are more and more de-correlated. The positive and negative oscillations in $\widehat{\boldsymbol{D}}_l$ are only evident for larger bubbles in the lower turbulent fields, or at low turbulence intensity $\beta = \frac{u'}{V_T}$. For 400 $\mu$m bubbles in field 3, $\beta \approx .2$. Both Mazzitelli and Lohse [20] and Spelt and Biesheuvel[13] observed similar behavior in bubble diffusivities and velocity correlation functions at low turbulence intensity, respectively with $\beta$ of about 0.5 and 0.1.

Analysis of the generalized dispersion coefficient in the transverse direction for 400 $\mu$m bubbles, shown in Figure 28, reveals oscillatory behavior for fields 3 and 4, whereas for fields 1 and 2 $\widehat{\boldsymbol{D}}_t$ decays in nearly monotonic fashion. However, contrary to the observed longitudinal behavior, small wavenumber limits are observed in all cases, suggesting that dispersion in the transverse direction can be approximated as a convolution-Fickian process at small times, and as Fickian process at larger times.

Figure 29 shows the the two-time velocity correlations for 400 $\mu$m bubbles in the transverse and longitudinal directions, again plotted in terms of the non-dimensional time lag. Contrary to the behavior of the 40 $\mu$m bubbles (Figure 26), the two-time velocity correlations of the 400 $\mu$m bubbles show significant dependence on the turbulence level. The dependence of the velocity correlations on turbulence intensity is consistent with earlier observations for the generalized dispersion coefficients.

# 5 Conclusions

Rise and dispersion of air bubbles in water under isotropic turbulence conditions are analyzed using a simplified one-way coupling model. The model combines DNS of single-phase flow, with a Lagrangian equation of motion for bubble dynamics. The latter accounts for drag, lift, pressure and added mass effects. The analysis assumes normal gravity conditions, and considers bubble radii ranging from 10-600 $\mu$m and dissipation rates in the range $10^{-5}$ – 0.3 $m^2/s^3$.

A statistical analysis is first conducted of the rise of microscopic bubbles, and of forces affecting their motion. In particular, the analysis indicates that:

1. The mean rise of the microbubbles is suppressed by turbulence, and the amount of suppression increases as the turbulence intensity increases. The results are thus consistent with established trends, and particularly with available computational[1] and experimental[2;3] data under relevant flow conditions.

2. Consistent with the analyses of Spelt and Biesheuvel[2] and Mazzitelli *et al.*[32], the suppression of the bubble rise velocity is promoted by lift force experience, which tend to move bubbles to regions of downward velocity. This effect is more pronounced as the bubble size increases.

3. Consistent with the experimental measurements of Poorte and Biesheuvel [3], in all cases considered the pdfs of the transverse bubble velocity are centered around 0, symmetric and nearly Gaussian. The pdfs of the vertical bubble velocity are generally asymmetric, and may be positively or negatively biased according to the turbulence intensity and Taylor scale. The variance of the vertical and transverse velocity pdfs increases as the turbulence level increases.

4. At low turbulence levels, the pdfs of the bubble Reynolds number (relative velocity) pdfs are nearly symmetric. As the dissipation rate increases, these pdfs become asymmetric and their variance increases. The mean bubble Reynolds numbers in turbulence are slightly smaller than the corresponding quiescent values.

5. At low turbulence levels, the pdfs of vorticity experienced by the bubbles are nearly identical to the vorticity pdf of the mean flow, and this close agreement occurs across the entire range of bubble radii considered in the analysis. At high turbulence levels, the vorticity pdfs for tiny bubbles remain close to that of the mean flow, whereas large bubbles have significantly broader pdfs. This trend is consistent with the observation that tiny bubbles have small slip velocities, and consequently tend to behave as Lagrangian markers, whereas larger bubbles are more easily captured by turbulent eddies, and thus experience higher vorticity.

6. The mean lift force experienced by the bubbles is a small fraction of the mean drag force, though this fraction increases as turbulence intensity

and bubble radius increase. The mean drag force in high turbulence is noticeably less than in low turbulence, which is consistent with suppression of the mean rise velocity. For bubbles smaller than 120 $\mu$m, the pdf of the vertical lift force is nearly symmetric and centered around 0, for all turbulence levels considered. As the turbulence level increases, the vertical lift pdfs become asymmetric and develop a positive mean. This behavior is consistent with increased likelihood of trapping of the bubbles on the downflow side of concentrated vortices, which would lead to the observed bias.

Analysis of bubble dispersion is conducted using a generalized length and time scale dependent model that can capture anomalous diffusion, convolution-Fickian, and classical Fickian behaviors. The model is an adapted from the theory developed by Cushman and Moroni[17]. A small wavenumber analysis is first conducted, which enables us to connect, when appropriate, the generalized dispersion predictions with classical dispersion results. Application of the generalized dispersion model to the computed bubble trajectories indicates that:

7. For 40 $\mu$m bubbles, the dispersion process is initially anomalous, but transitions to Fickian over a time span that scales with the integral time scale of turbulence. This trend persists for the entire range of turbulence levels considered in the analysis.

8. For 400 $\mu$m bubbles, a qualitatively similar behavior is observed for high turbulence levels. In particular, transition to Fickian dispersion occurs over similar time scales as the 40 $\mu$m bubbles. At low turbulence levels, however, oscillations are observed in the generalized dispersion coefficients, which also exhibit dependence on spatial lengthscales. Thus, in these situations, transition to Fickian dispersion is not observed within the time span of the analysis.

## Acknowledgments

This research was funded by the Department of Energy and by the United States Naval Academy (via the Permanent Military Professor program).

# References


[1] L.P. Wang and M.R. Maxey. The motion of microbubbles in a forced isotropic and homogeneous turbulence. *Applied Science Research*, 51:291–296, 1993.

[2] P.D.M. Spelt and A. Biesheuvel. On the motion of gas bubbles in homogeneous isotropic turbulence. *Journal of Fluid Mechanics*, 336:221–244, 1997.

[3] R.E.G. Poorte and A. Biesheuvel. Experiments on the motion of gas bubbles in turbulence generated by an active grid. *Journal of Fluid Mechanics*, 461:127–154, 2002.

[4] M.R. Maxey. The gravitational settling of aerosol particles in homogeneous turbulence and random flow fields. *Journal of Fluid Mechanics*, 174:441–465, 1987.

[5] L.P. Wang and M.R. Maxey. Settling velocity and concentration distribution of heavy particles in homogeneous isotropic turbulence. *Journal of Fluid Mechanics*, 256:27–68, 1993.

[6] R. Mei. Flow due to an oscillating sphere and an expression for unsteady drag on the sphere at finite reynolds number. *Journal of Fluid Mechanics*, 270:133–174, 1994.

[7] E.B. Tunstall and G. Houghton. Retardation of falling spheres by hydrodynamic oscillations. *Chemical Engineering Science*, 23:1067–1081, 1968.

[8] P.A. Hwang. Fall velocity of particles in oscillating flow. *Journal of Hydraulic Engineering*, 111:485–502, 1985.

[9] J.C.H. Fung. Gravitational settling of particles and bubbles in homogeneous turbulence. *Journal of Geophysical Research*, 98:20287–20297, 1993.

[10] J.C.H. Fung. Effect of nonlinear drag on the settling velocity of particles in homogeneous isotropic turbulence. *Journal of Geophysical Research*, 103:27905–27917, 1998.

[11] J.E. Stout, S.P. Arya, and E.L. Genikhovich. The effect of nonlinear drag on the motion and settling velocity of heavy particles. *Journal of Atmospheric Sciencies*, 52:3836–3848, 1995.

[12] R. Mei, R.J. Adrian, and T.J. Hanratty. Turbulent dispersion of heavy particles with nonlinear drag. *Transactions of the ASME: Journal of Fluids Engineering*, 119:170–179, 1997.

[13] P.D.M. Spelt and A. Biesheuvel. Dispersion of gas bubbles in large-scale homogeneous isotropic turbulence. *Applied Scientific Research*, 58:463–482, 1998.

[14] P.D. Friedman and J. Katz. Mean rise rate of droplets in isotropic turbulence. *Physics of Fluids*, 14(9):3059–3073, 2002.

[15] W.L. Haberman and R.K. Morton. An experimental study of bubbles moving in liquids. *Transactions of the American Society of Civil Engineers*, 387:227–252, 1954.

[16] G. Sridhar and J. Katz. Drag and lift forces on microscopic bubbles entrained by a vortex. *Physics of Fluids*, 7:389–399, 1995.

[17] J.H. Cushman and M. Moroni. Statistical mechanics with three-dimensional particle tracking velocity experiments in the study of anomalous dispersion. i. theory. *Physics of Fluids*, 13:75–80, 2001.

[18] M. Moroni and J.H. Cushman. Statistical mechanics with three-dimensional particle tracking velocity experiments in the study of anomalous dispersion. ii. experiments. *Physics of Fluids*, 13:81–91, 2001.

[19] W. Snyder and J. Lumley. Some measurements of particle velocity autocorrelation functions in a turbulent flow. *Journal of Fluid Mechanics*, 48:41–71, 1971.

[20] I.M. Mazzitelli and D. Lohse. Lagrangian statistics for fluid particles and bubbles in turbulence. *New Journal of Physics*, 6:203, 2004.

[21] G.K. Batchelor. *An Introduction to Fluid Dynamics*. Cambridge University Press, Cambridge, 1967.

[22] A. Vincent and M. Meneguzzi. The spatial structure and statistical properties of homogeneous turbulence. *Journal of Fluid Mechanics*, 256:1–20, 1991.

[23] C. Canuto, M.Y. Hussaini, A. Quarteroni, and T.A. Zang. *Spectral Methods in Fluid Dynamics*. Springer-Verlag, Berlin, 1987.

[24] S.A. Orszag. Numerical simulation of incompressible flows within simple boundaries. i. galerkin (spectral) representations. *Studies in Applied Mathematics*, 50:293–327, 1971.

[25] M.R. Maxey and J.J. Riley. Equation of motion for a small rigid sphere in a nonuniform flow. *Physics of Fluids*, 26:883–889, 1983.

[26] S. Cerutti, O. Knio, and J. Katz. Numerical study of cavitation inception in the near field of an axisymmetric jet at high reynolds number. *Physics of Fluids*, 12:2444–2460, 2000.

[27] G. Sridhar and J. Katz. Effect of entrained bubbles on the structure of vortex rings. *Journal of Fluid Mechanics*, 397:171–202, 1999.

[28] F.M. White. *Viscous fluid flow*. McGraw Hill, Boston, 2006.

[29] K.J. Sene, J.C.R. Hunt, and N.H. Thomas. The role of coherent structures in bubble transport by turbulent shear flows. *Journal of Fluid Mechanics*, 259:219–240, 1994.

[30] M.R. Maxey, E.J. Chang, and L.P. Wang. Simulation of interactions between microbubbles and turbulent flows. *Applied Mechanics Review*, 47:S70–S74, 1994.

[31] I.M. Mazzitelli and D. Lohse. The effect of microbubbles on developed turbulence. *Physics of Fluids*, 15:L5–L8, 2003.

[32] I.M. Mazzitelli, D. Lohse, and F. Toschi. On the relevance of the lift force in bubbly turbulence. *Journal of Fluid Mechanics*, 488:283–313, 2003.

[33] G.I. Taylor. Dispersion of soluble matter in solvent flowing slowly through a tube. *Proceedings of the Royal Society of London. Series A*, 219:186–203, 1953.

[34] G.I. Taylor. Conditions under which dispersion of a solute in a stream of solvent can be used to measure molecular diffusion. *Proceedings of the Royal Society of London. Series A*, 225:473–477, 1954.

[35] M.I. Yudine. Physical considerations on heavy-particle diffusion. *Advances in Geophysics*, 6:185–191, 1959.

[36] S. Corrsin. Estimates of the relations between eulerian and lagrangian scales in large reynolds number turbulence. *Journal of the Atmospheric Sciences*, 20:115–119, 1963.

| *Field* | 1 | 2 | 3 | 4 |
|---|---|---|---|---|
| $\widetilde{L}$ (m) | .0125 | .0250 | .090 | .157 |
| $L^c$ (m) | .00199 | .00398 | .014 | .025 |
| $U^c$ (m/s) | .503 | .251 | .070 | .04 |
| $\tilde{t^c}$ (s) | .00396 | .0159 | .200 | .625 |
| $\tilde{t_K}$ (s) | .00198 | .00791 | .102 | .313 |
| $\tilde{t_L}$ (s) | .0626 | .250 | 3.23 | 9.90 |
| $\tilde{\eta}$ ($\mu$m) | 44 | 88 | 315 | 550 |
| $\tilde{\lambda}$ ($\mu$m) | 828 | 1650 | 5960 | 10400 |
| $\tilde{\epsilon}$ (m$^2$/s$^3$) | .256 | .016 | $9.58 \times 10^{-5}$ | $1.02 \times 10^{-5}$ |
| $g$ | .077 | .617 | 28.6 | 153. |

Table 1: Turbulent Fields Modeled. $\widetilde{L}$ is the side length of the domain, $L^c$ is the characteristic length scale, $U^c$ is the characteristic velocity, $\tilde{t^c} \equiv L^c/U^c$ is the characteristic time scale, $\tilde{t_K} = \sqrt{\tilde{\nu}/\tilde{\epsilon}}$ is the Kolmogorov time scale, $\tilde{t_L} = \tilde{t_K} Re^{1/2}$ is the integral time scale, $\tilde{\eta}$ is the Kolmogorov microscale, $\tilde{\lambda} = \sqrt{15\tilde{\nu}u'^2/\tilde{\epsilon}}$ is the Taylor length scale, $\tilde{\epsilon}$ is the dissipation rate, and $g$ is the dimensionless gravity.

| Bubble Radius | Field 1 | Field 2 | Field 3 | Field 4 |
|---|---|---|---|---|
| 240 $\mu$m | .37 | .62 | .77 | .83 |
| 400 $\mu$m | .38 | .59 | .82 | .82 |

Table 2: Ratio of the mean turbulent rise velocity and the quiescent rise velocity.

| | Field 1 | Field 2 | Field 3 | Field 4 |
|---|---|---|---|---|
| With Lift | .37 | .62 | .77 | .83 |
| Zeroed Lift | .39 | .66 | .81 | .84 |

Table 3: Observed rise velocity for 240 $\mu$m bubbles in turbulence as a fraction of quiescent rise velocity (with lift, top row, and zeroed lift, bottom row).

| Bubble Radius | Field 1 | Field 2 | Field 3 | Field 4 |
|---|---|---|---|---|
| 120 $\mu$m | 4.15% | .0348% | .447% | .176% |
| 240 $\mu$m | 9.97% | 1.29% | .450% | .381% |
| 400 $\mu$m | 14.7% | 1.68% | 1.51% | .936% |
| 500 $\mu$m | 15.6% | 1.15% | 2.34% | 1.48% |

Table 4: Ratio $\langle L \rangle \,/\, \langle D \rangle$ of the mean total lift and drag forces.

| Bubble Radius | Field 1 | Field 2 | Field 3 | Field 4 |
|---|---|---|---|---|
| 120 $\mu$m | .0415 | $-.000112$ | $-0.00705$ | $-0.00176$ |
| 240 $\mu$m | .0999 | .0129 | $-0.00458$ | $-0.00129$ |
| 400 $\mu$m | .147 | .0168 | $-0.0150$ | $-0.00939$ |
| 500 $\mu$m | .156 | .0114 | $-0.0233$ | $-0.0148$ |

Table 5: Mean lift force in the vertical direction $\langle L_z \rangle$ normalized by mean magnitude of drag force $\langle |D| \rangle$.

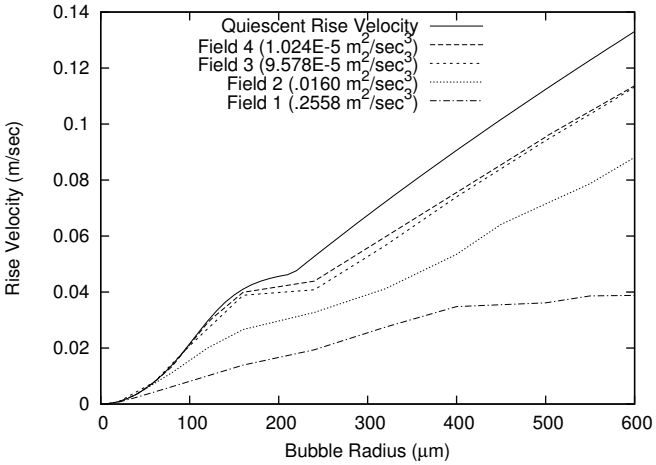


Figure 1: Mean rise velocity of bubbles in turbulence. Predictions for quiescent flow are also plotted.

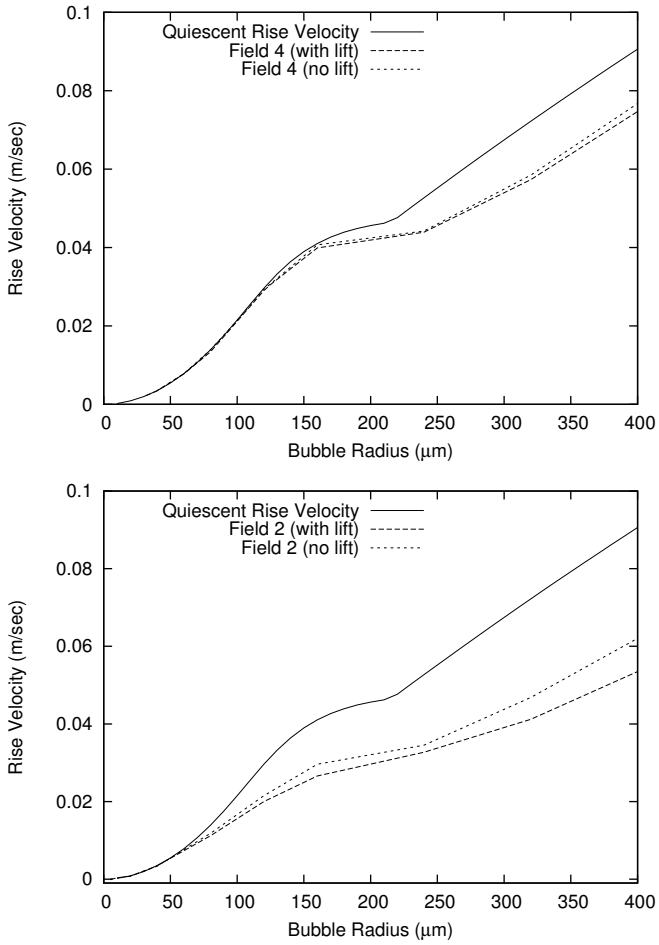


Figure 2: Mean rise velocity in turbulence versus bubble radius with experimental $C_L$ and zero lift. Top: results for field 4; bottom: results for field 2. Predictions for quiescent flow are also plotted. In both fields, the bubbles rise faster when the lift force is ignored.

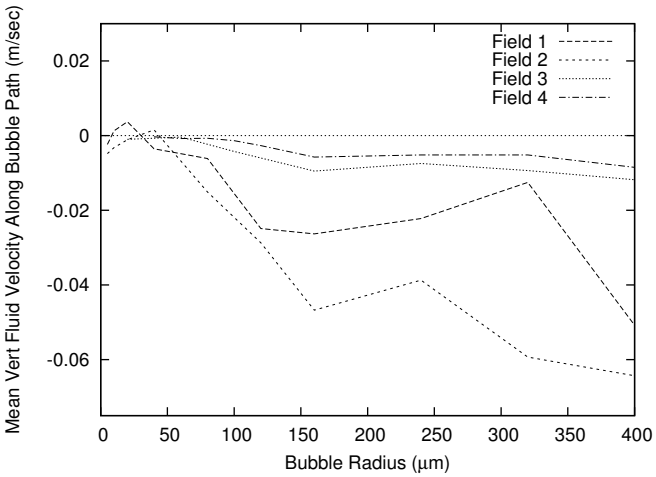


Figure 3: Mean vertical fluid velocity along the bubble path versus the bubble radius.

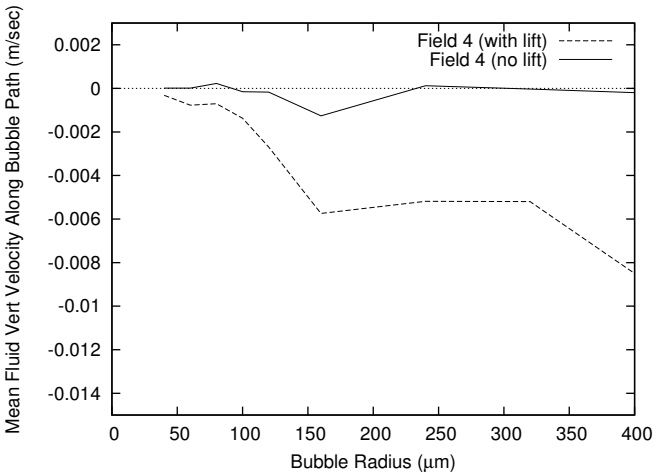


Figure 4: Mean vertical fluid velocity along the bubble path. Shown are results for field 4 with $C_L = 0$ and the experimental $C_L$.

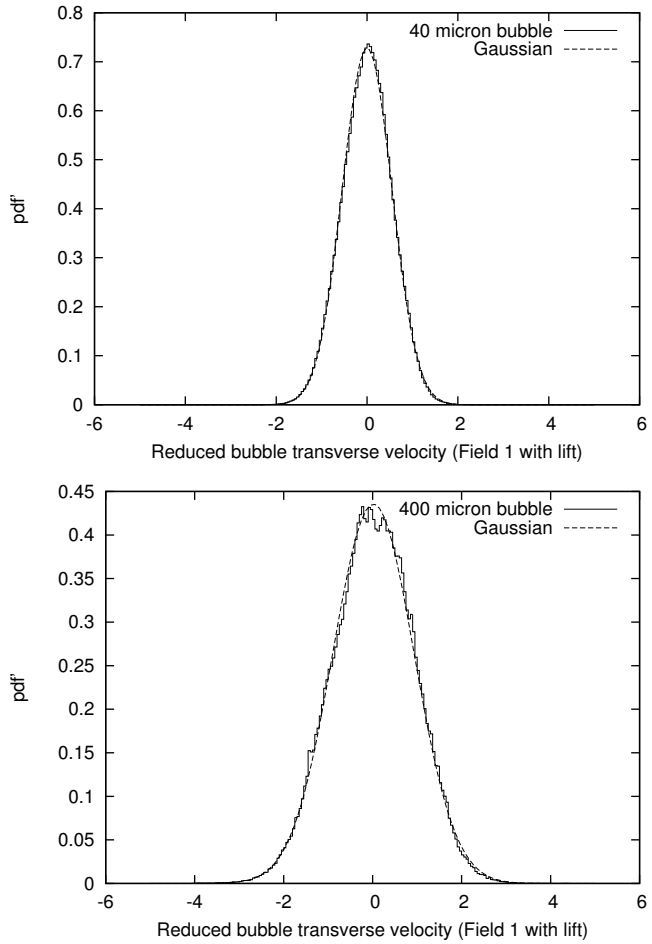


Figure 5: Pdfs of the bubble transverse velocity for 40 $\mu$m (top) and 400 $\mu$m (bottom) bubbles in field 1.

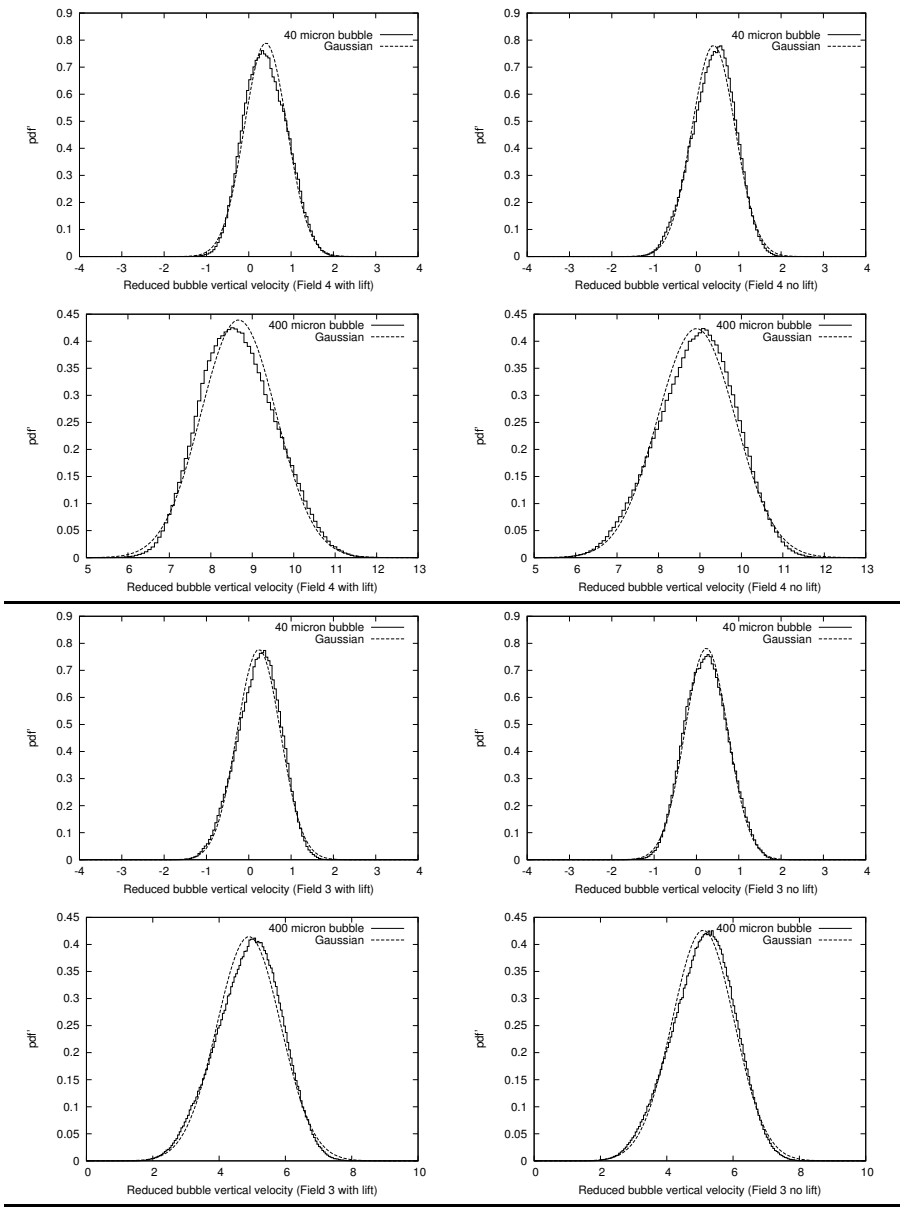


Figure 6: Pdfs of the bubble vertical velocity pdfs for 40 $\mu$m and 400 $\mu$m bubbles in field 4 (rows 1 and 2) and field 3 (rows 3 and 4). Plotted on the left column are results obtained with experimental $C_L$, and on the right column predictions with $C_L = 0$.

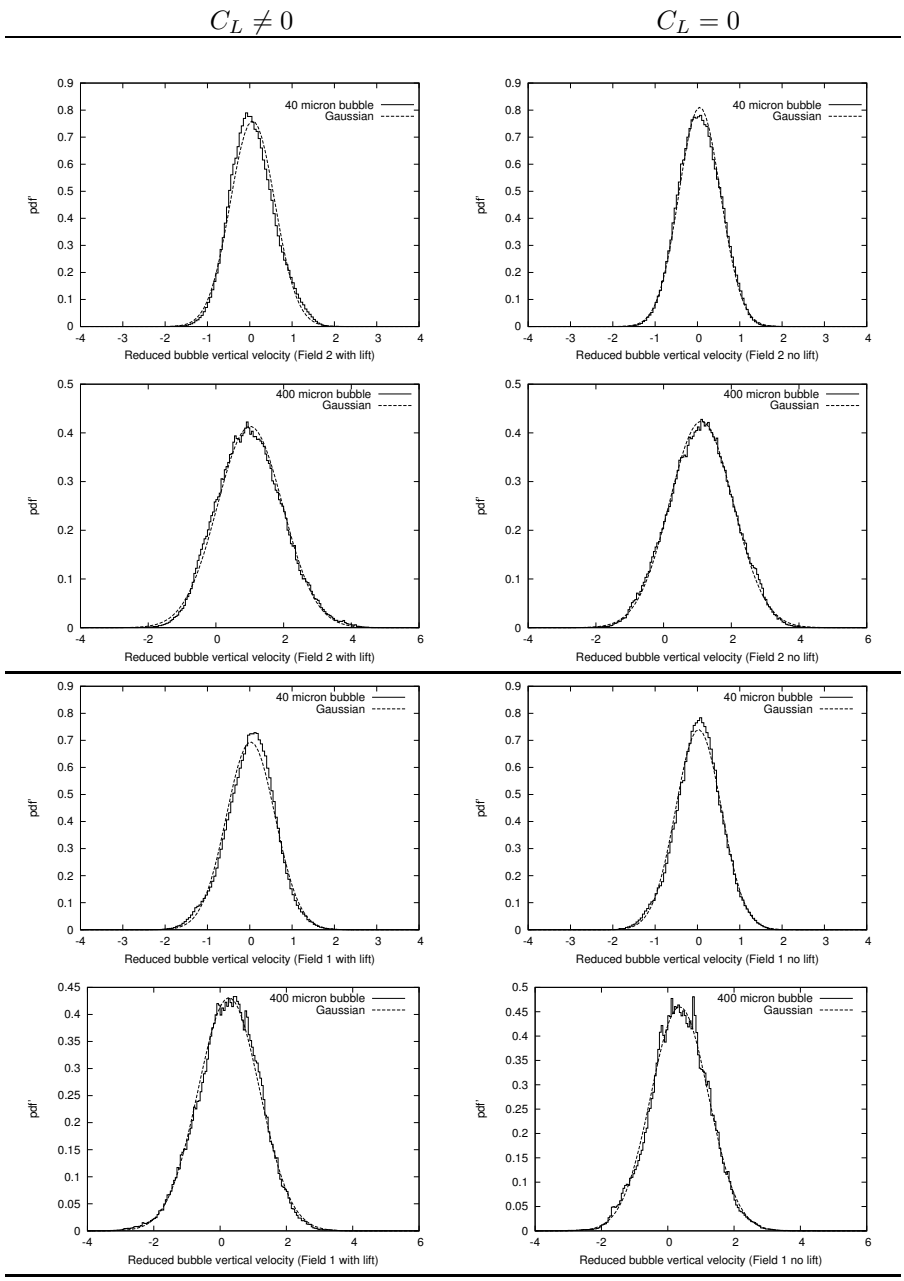


Figure 7: Pdfs of the bubble vertical velocity pdfs for 40 $\mu$m and 400 $\mu$m bubbles in field 2 (rows 1 and 2) and field 1 (rows 3 and 4). Plotted on the left column are results obtained with experimental $C_L$, and on the right column predictions with $C_L = 0$.

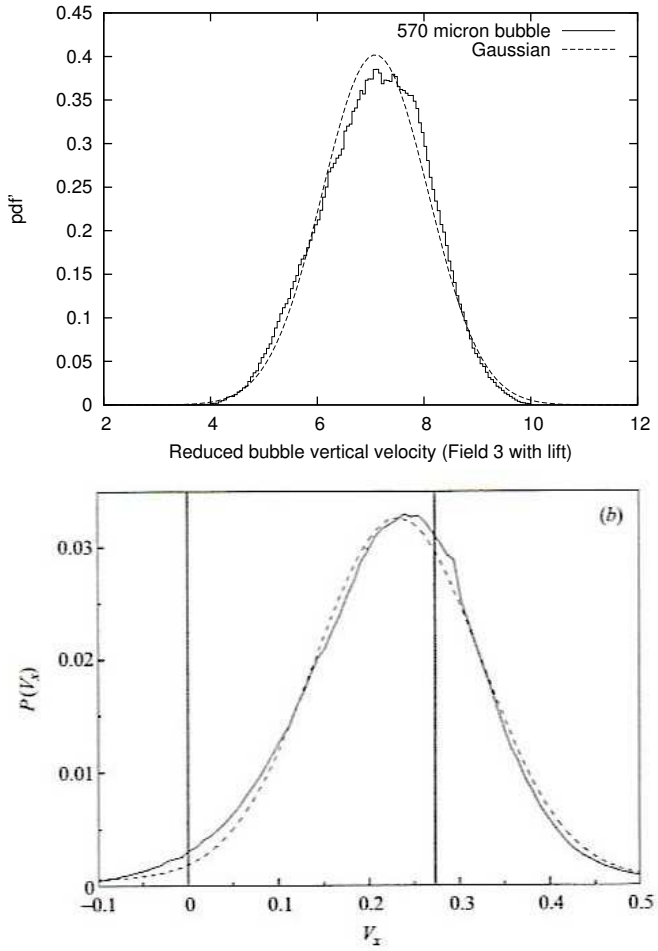


Figure 8: Top: computed pdfs of the normalized bubble vertical velocity for 570 $\mu$m bubble in field 3 ($\beta = 0.17$ and $\lambda^* = 0.72$). Bottom: experimental results of Poorte and Biesheuvel[3] for 570 $\mu$m bubbles with $\beta = 0.21$ and $\lambda^* = 0.54$ (solid line is pdf of vertical velocity, dashed line is Gaussian, left vertical line is zero vertical velocity, and right vertical line is rise velocity in still fluid).

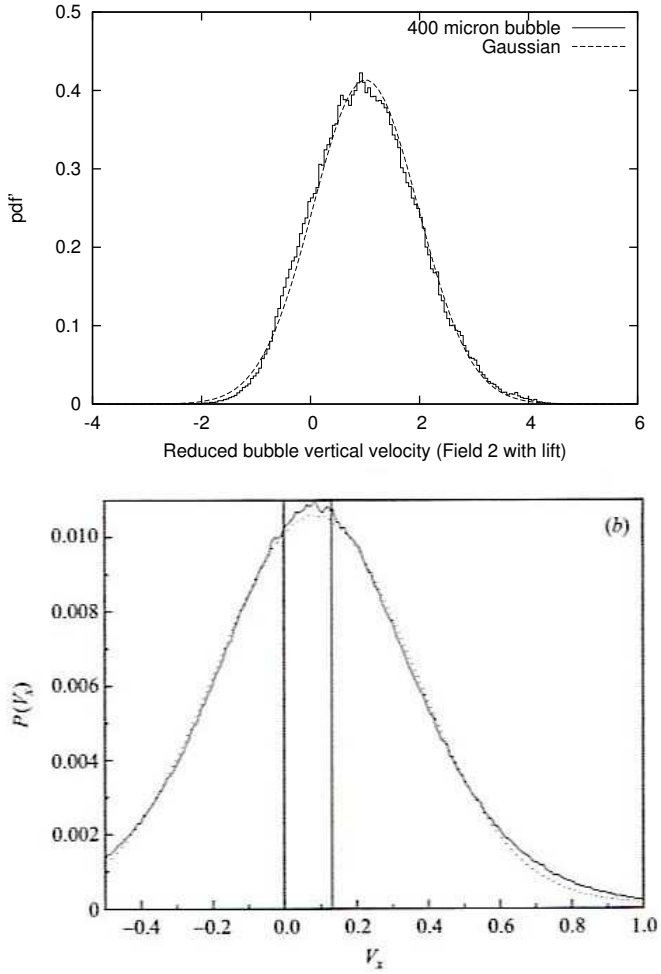


Figure 9: Top: computed pdfs of the normalized bubble vertical velocity for 400 $\mu$m bubble in field 2 ($\beta = 0.60$ and $\lambda^* = 3.99$). Bottom: experimental results of Poorte and Biesheuvel[3] for 340 $\mu$m bubbles with $\beta = 0.44$ and $\lambda^* = 3.56$ (solid line is pdf of vertical velocity, dashed line is Gaussian, left vertical line is zero vertical velocity, and right vertical line is rise velocity in still fluid).

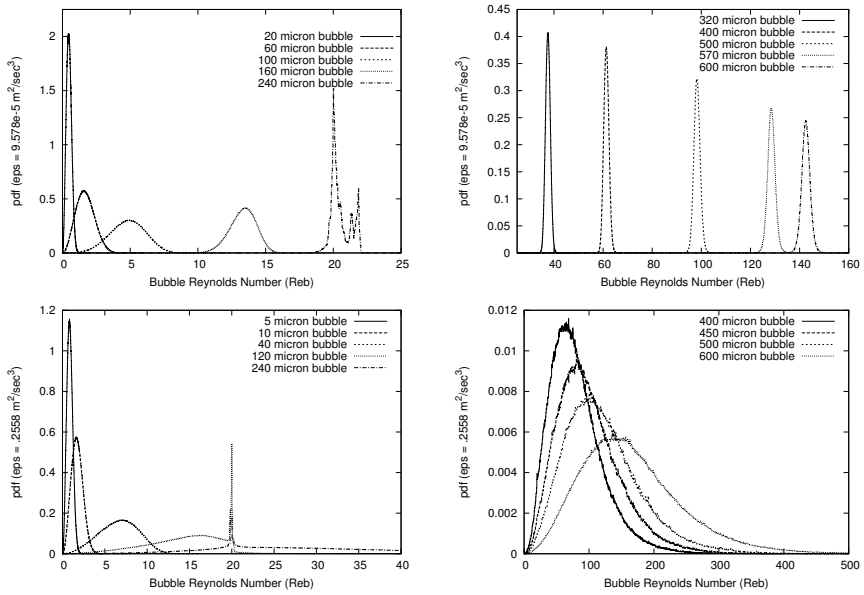


Figure 10: Pdfs of the bubble Reynolds number pdfs for field 3 (top) and field 1 (bottom). The bubble radius is indicated.

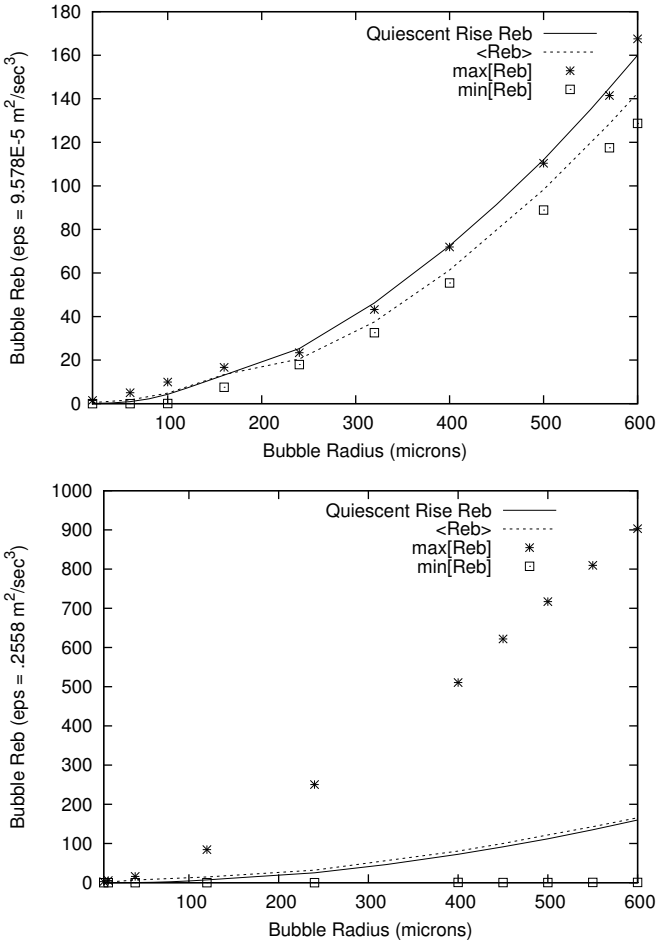


Figure 11: Maximum, mean, minimum, and quiescent rise bubble Reynolds number versus bubble radius for field 3 (top) and field 1 (bottom). Note the difference in $Re_b$ scales.

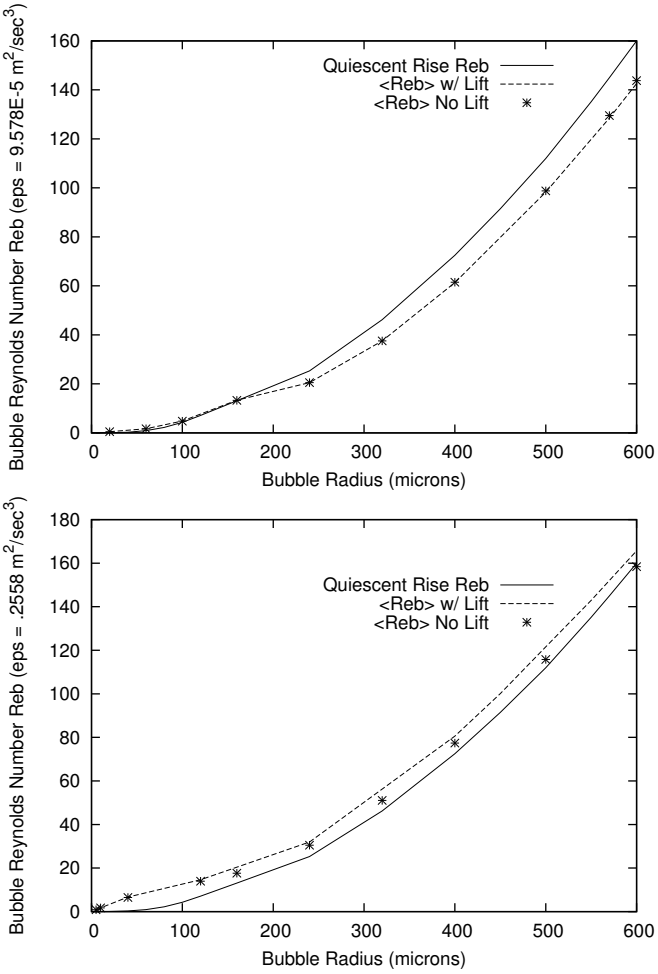


Figure 12: Mean and quiescent rise bubble Reynolds number versus radius for field 3 (top) and field 1 (bottom). Results with experimental lift and $C_L = 0$ are shown.

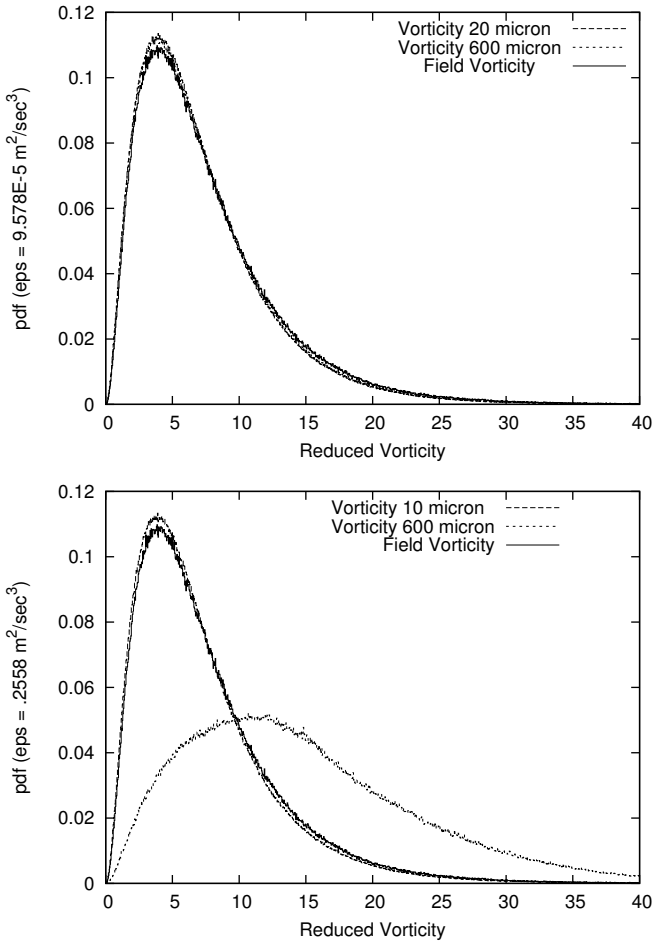


Figure 13: Pdf of the normalized vorticity felt by bubbles for field 3 (top) and field 1 (bottom). The pdf of the normalized field vorticity is also plotted for comparison.

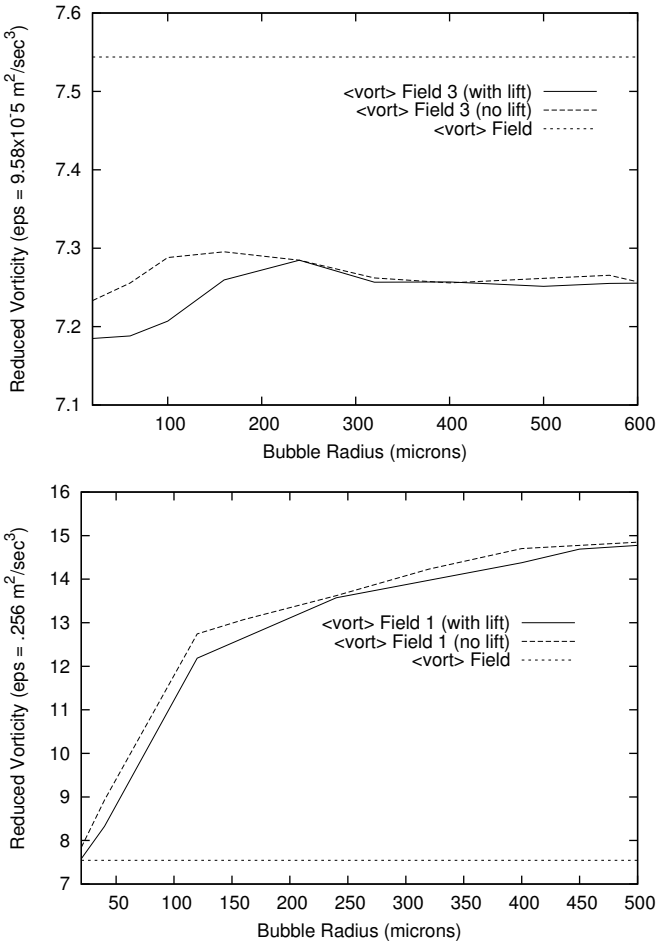


Figure 14: Mean normalized vorticity versus bubble radius for field 3 (top) and field 1 (bottom). Plotted are results obtained using experimental $C_L$ and $C_L = 0$.

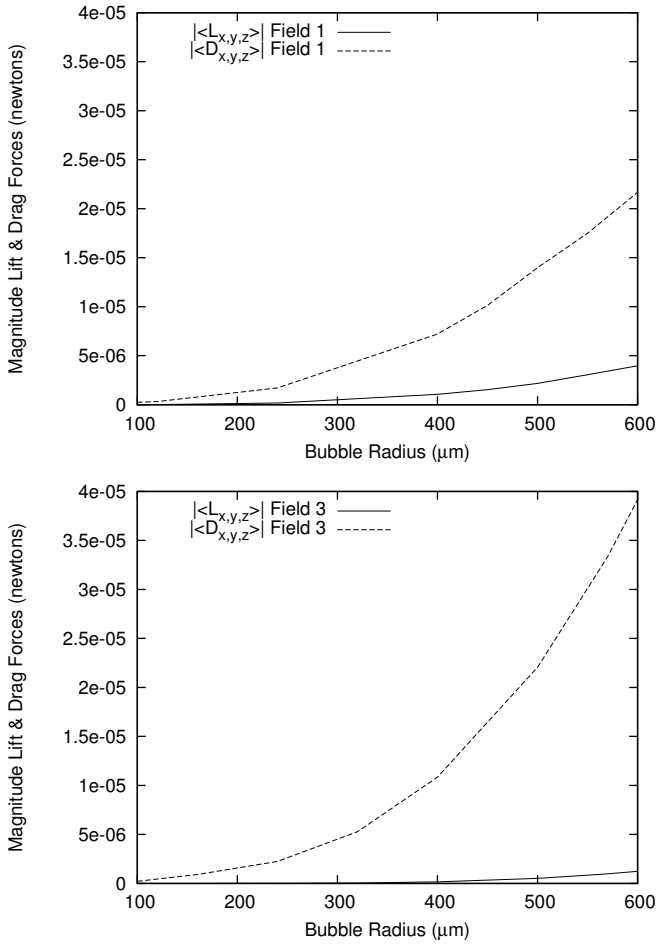


Figure 15: Magnitude of total mean lift force $\langle L \rangle$ and magnitude of total mean drag force $\langle D \rangle$ in field 1 (top) and field 3 (bottom).

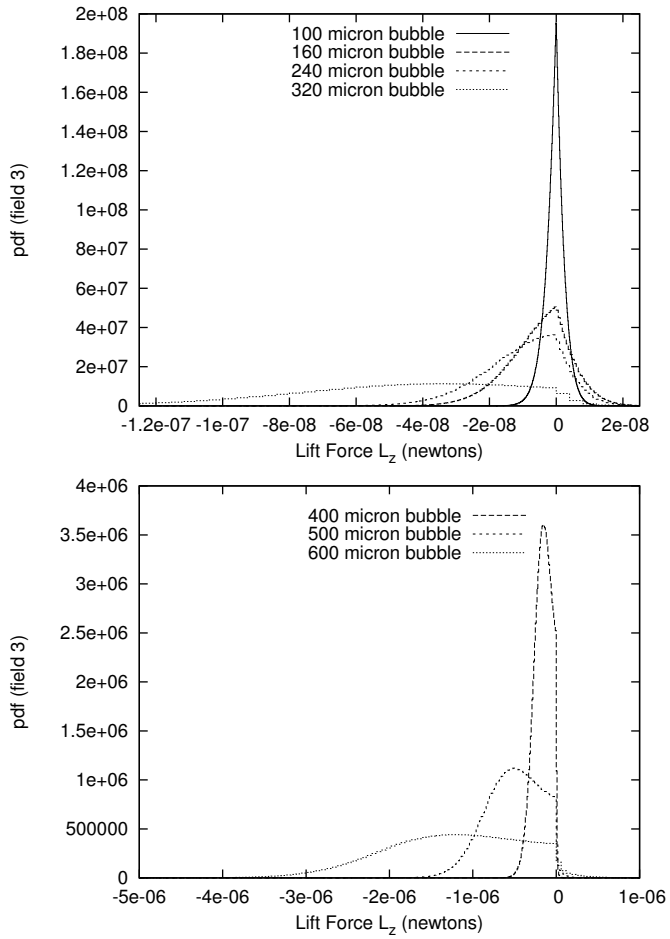


Figure 16: Pdfs of the vertical component of the lift force, $L_z$, in field 3.

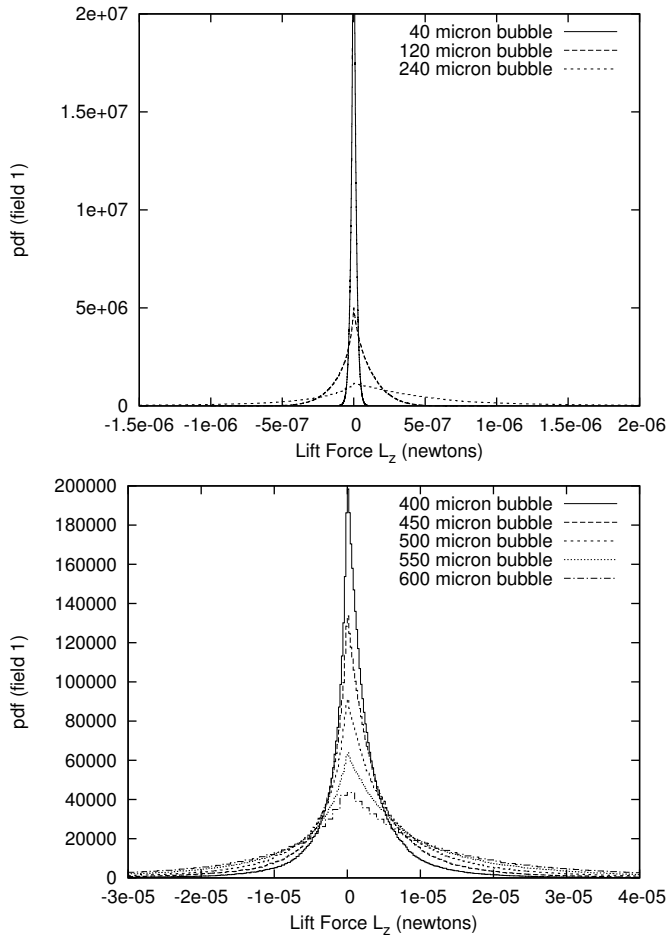


Figure 17: Pdfs of the vertical component of the lift force, $L_z$, in field 1.

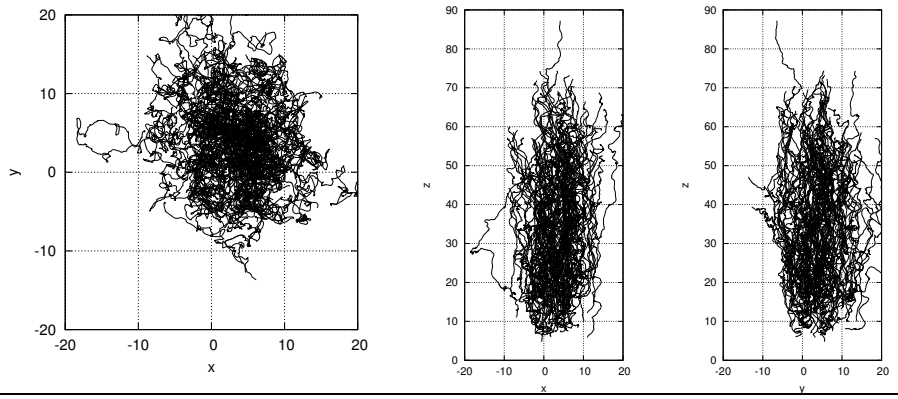


Figure 18: Trajectories of 400 $\mu$m bubbles in field 2. The trajectories of 100 bubbles are plotted. Left plot: top view. Middle and right plots: side-views.

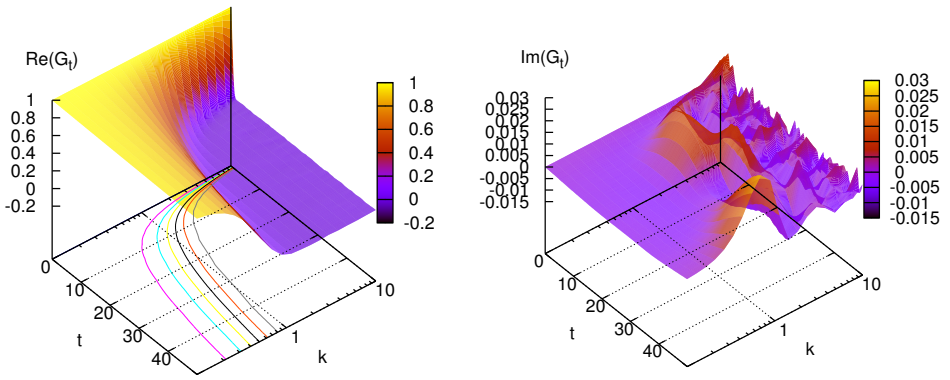


Figure 19: Real (left) and imaginary (right) part of $\widehat{G}_t(k,t)$ (equation (49)) for 400 $\mu$m bubbles in field 2.

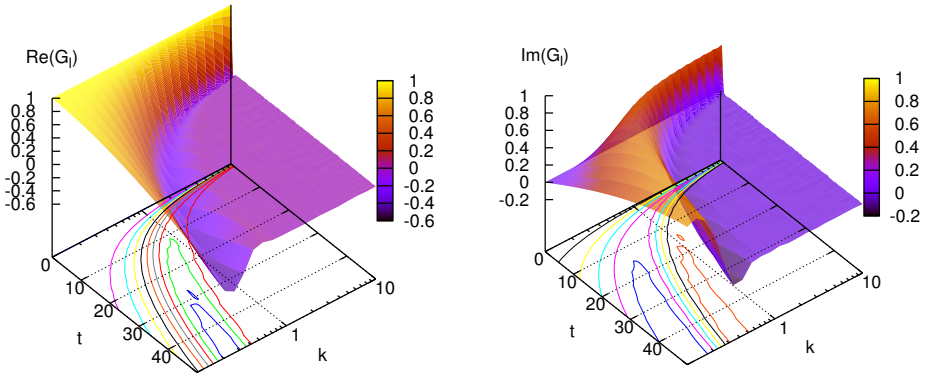


Figure 20: Real (left) and imaginary (right) part of $\widehat{G}_l(k,t)$ (equation (49)) for 400 $\mu$m bubbles in field 2.

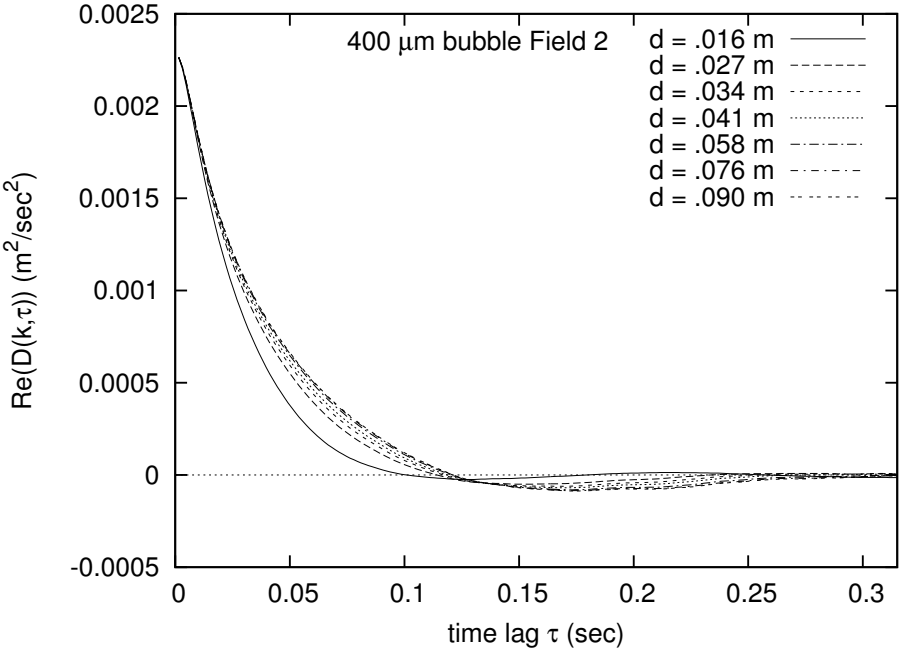


Figure 21: Real part of $\widehat{\boldsymbol{D}}_t$ for 400 $\mu$m bubbles in field 2 $\left(d = \frac{2\pi}{k}\right)$.

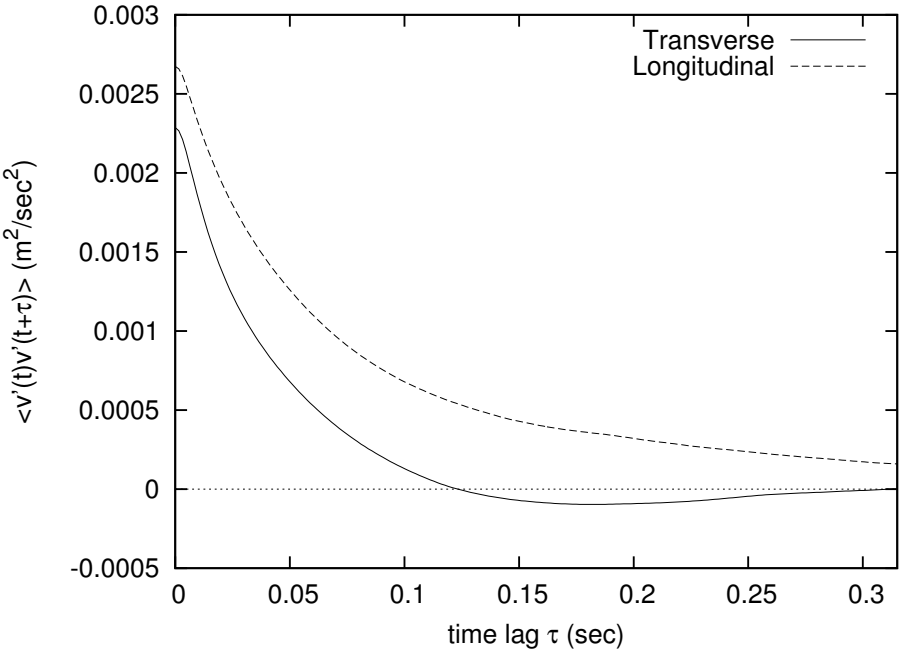


Figure 22: Velocity correlation in transverse and longitudinal directions for 400 $\mu$m bubbles in field 2.

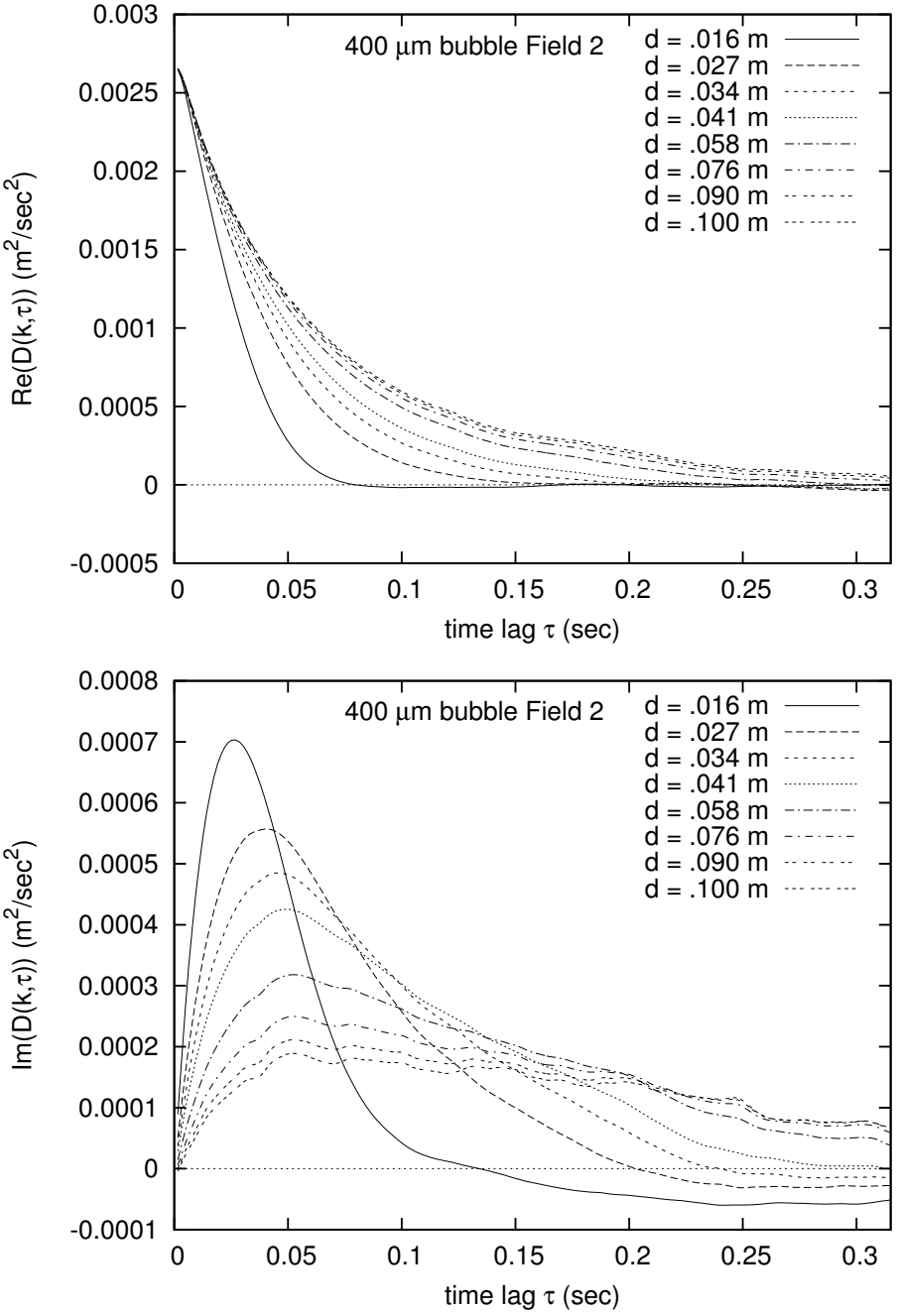


Figure 23: Real (top) and imaginary (bottom) component of the generalized dispersion tensor $\widehat{\boldsymbol{D}}_l$ in the longitudinal direction for 400 $\mu$m bubbles in field 2 $\left(d = \frac{2\pi}{k}\right)$.

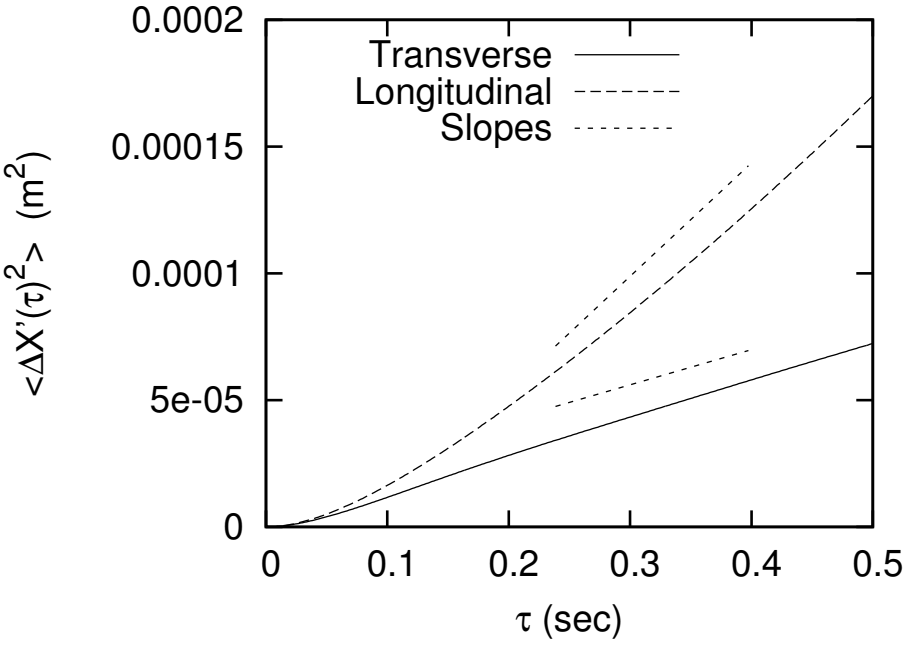


Figure 24: Evolution of the variance of the transverse and longitudinal displacements. Also shown are the slopes, *i.e.* $d\left\langle \Delta \boldsymbol{X}'^2 \right\rangle / d\tau$, predicted from the time integration of $\widehat{\boldsymbol{D}}_{t,l}$ (equation (46)) for $k = 0.1$.

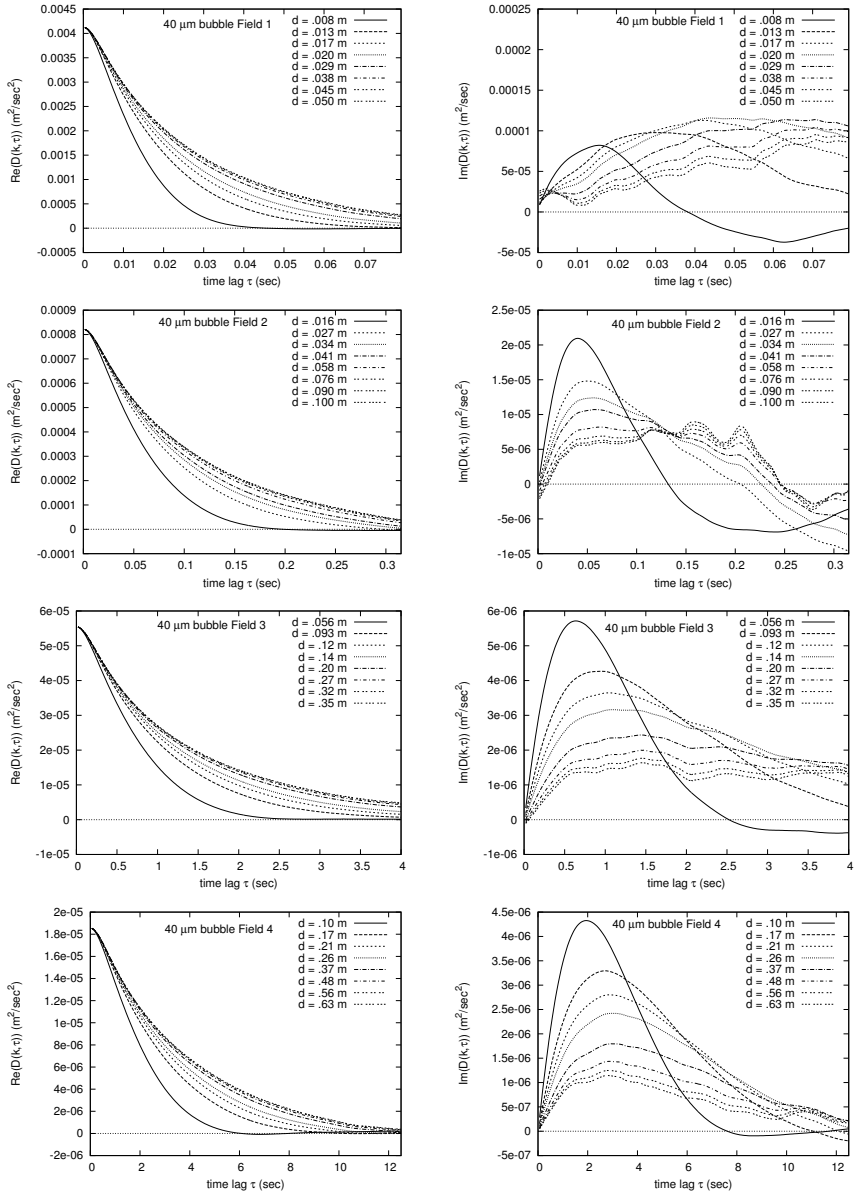


Figure 25: Real (left) and imaginary (right) parts of generalized dispersion coefficients in longitudinal direction for 40 $\mu$m bubbles in fields 1-4 $\left(d = \frac{2\pi}{k}\right)$.

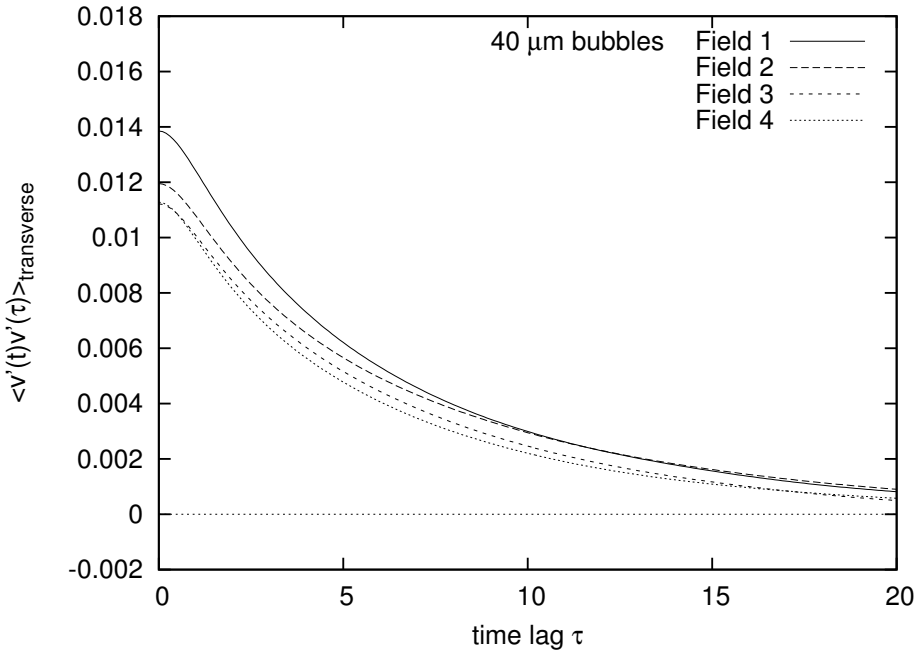


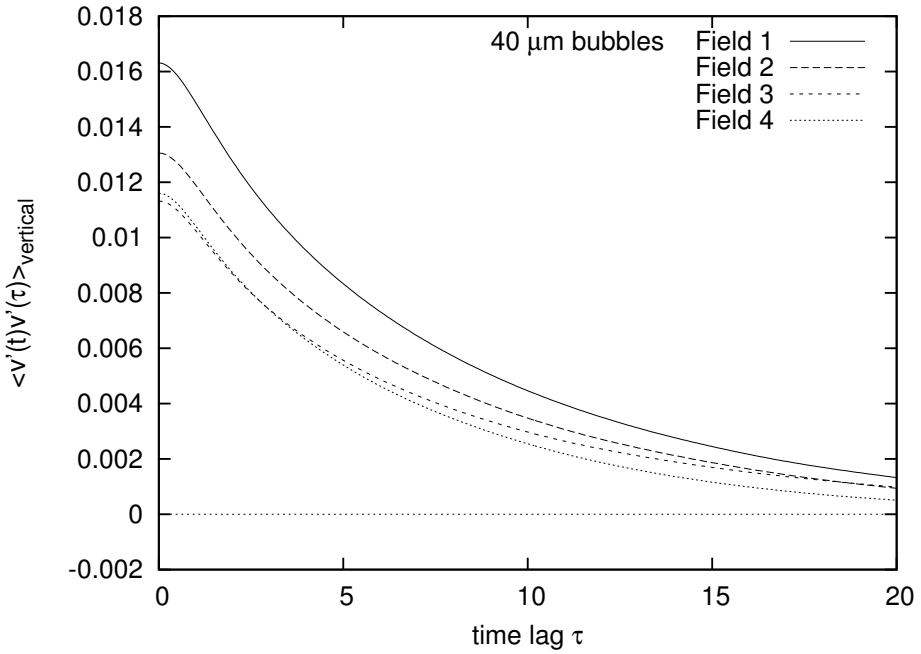


Figure 26: $\langle v'(t)v'(\tau)\rangle$ in the transverse (top) and longitudinal (bottom) direction for 40 $\mu$m bubbles in fields 1-4.

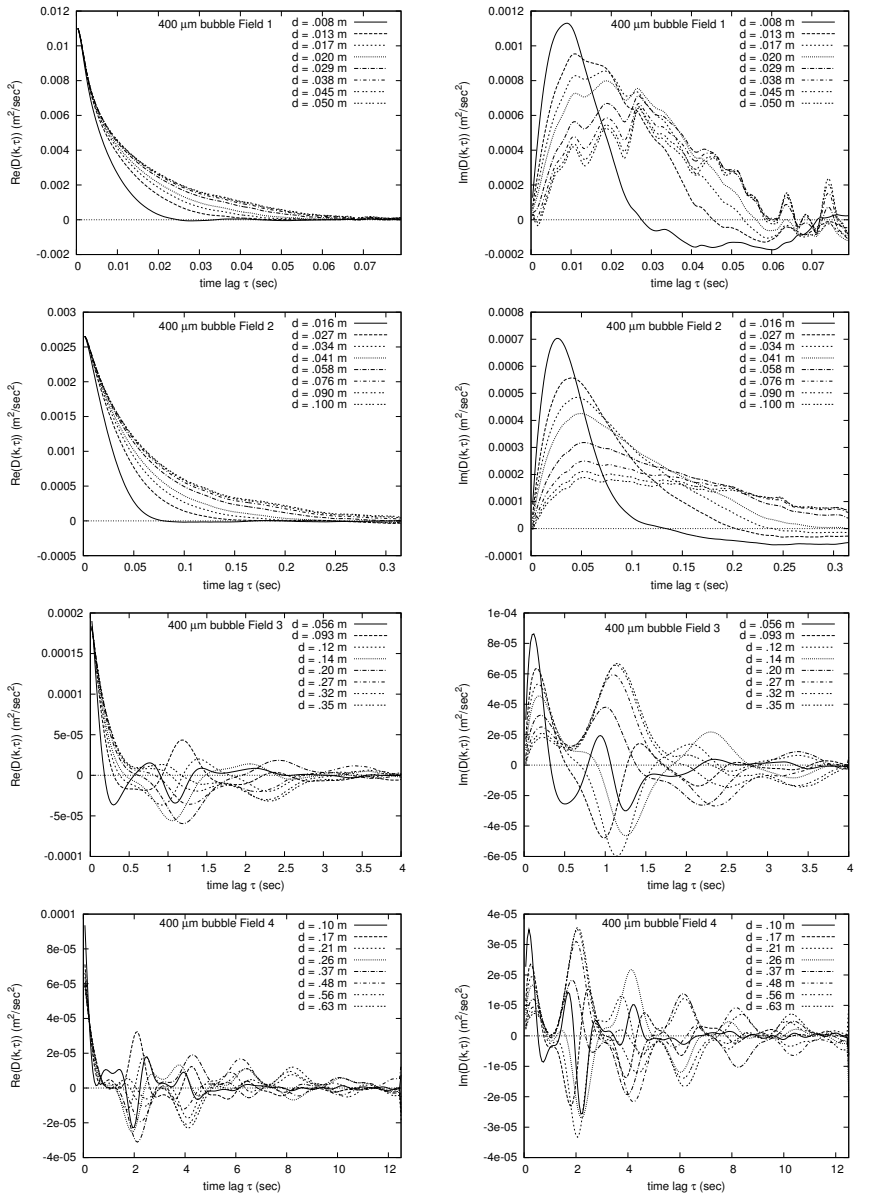


Figure 27: Real (left) and imaginary (right) parts of generalized dispersion coefficients in longitudinal direction for 400 $\mu$m bubbles fields 1-4 $\left(d = \frac{2\pi}{k}\right)$.

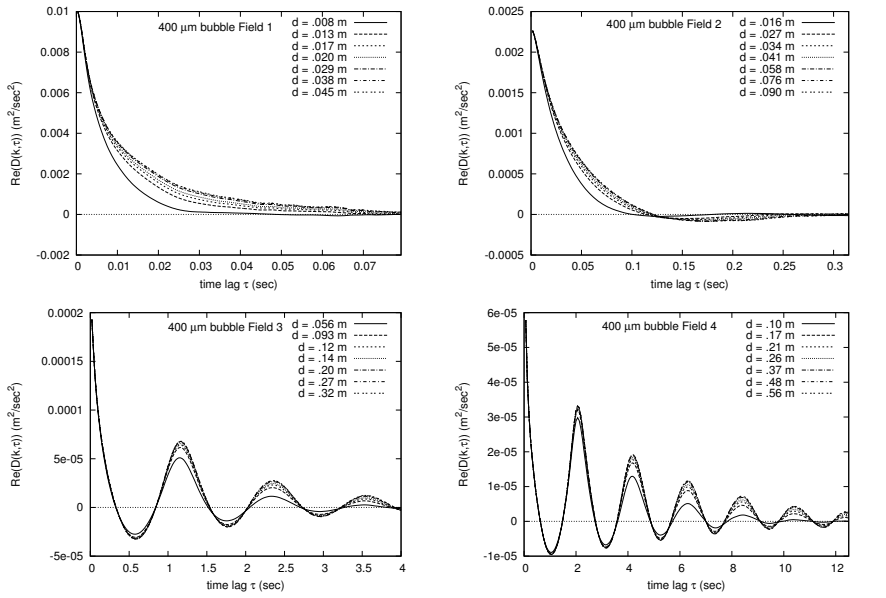


Figure 28: Real component of generalized dispersion tensor $Re(\mathbf{D})$ in transverse direction for 400 $\mu$m bubbles (field 1 upper left, field 2 upper right, field 3 lower left, field 4 lower right) $\left(d = \frac{2\pi}{k}\right)$.

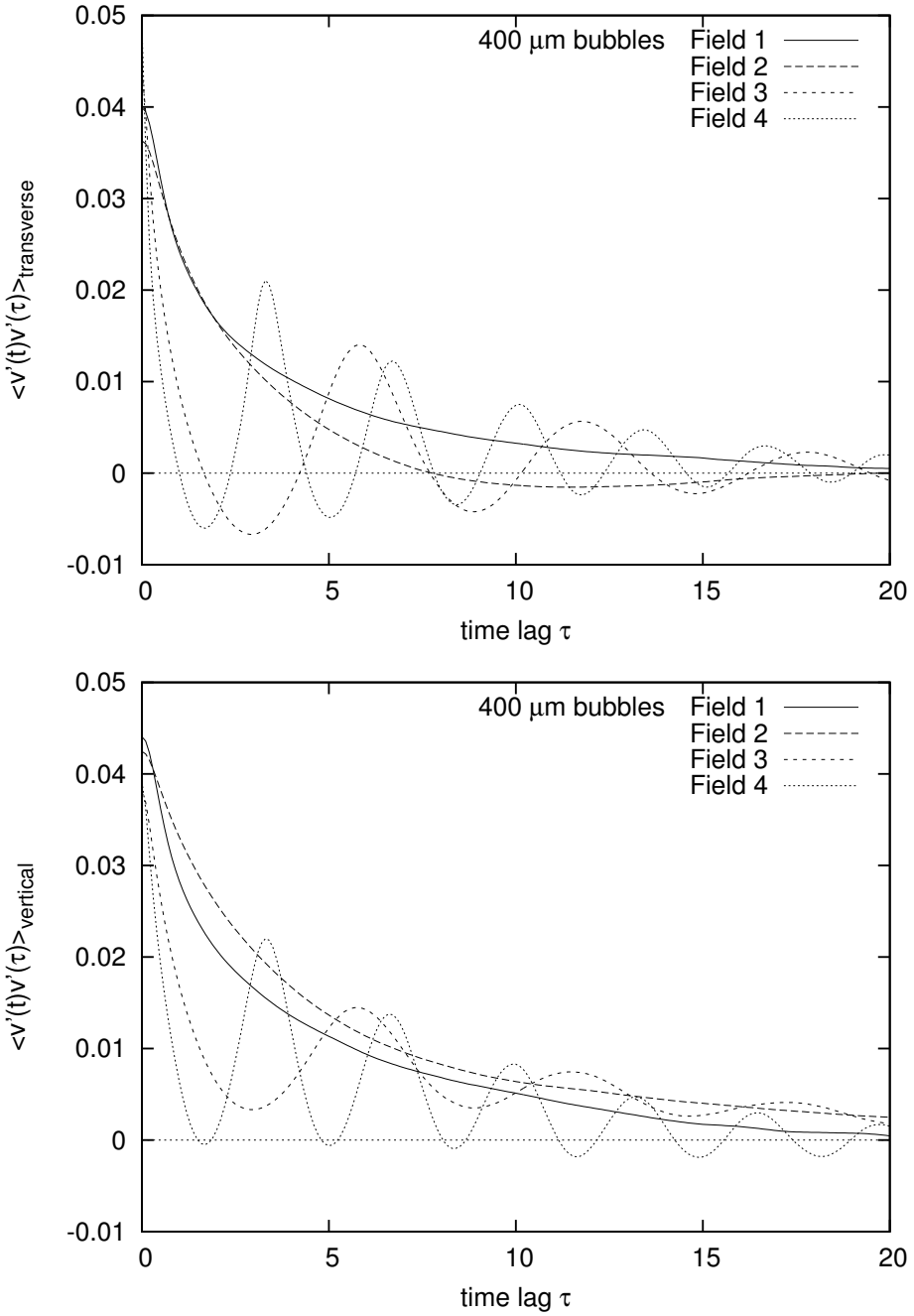


Figure 29: $\langle v'(t)v'(\tau)\rangle$ in the transverse direction (top) and in the longitudinal direction (bottom) for 400 $\mu$m bubbles in all fields.